Horizontal Lines of Nodes in the Superconducting Gap of Sr_2RuO_4: Evidence against the Anticipated Chiral *p*-wave Scenario

Sakakibara Group

The layered-perovskite superconductor Sr_2RuO_4 has been a leading candidate of a spin-triplet chiral *p*-wave superconductor; the spin-triplet pairing (chiral state) was suggested by the invariant spin susceptibility across T_c (time-reversal symmetry breaking in the superconducting state) [1]. However, the recently-discovered first-order superconducting transition, reminiscent of the Pauli-paramagnetic effect, under an in-plane magnetic field is likely to favor the spin-singlet scenario [2, 3]. Moreover, whereas symmetry-protected nodes are forbidden in the spin-triplet scenario, the presence of nodes has been suggested from various thermodynamic experiments. Thus, the order parameter of Sr_2RuO_4 has remained controversial.

Recently, we have developed field-angle-resolved measurements of the specific heat as a powerful technique to identify the superconducting gap structure [4]. Here, in order to provide hints for resolving the puzzling issues on Sr_2RuO_4, we have performed the field-angle-resolved measurements at low temperatures down to 0.06 K by using a high-quality single crystal (T_c = 1.505 K) [5]. By subtracting the Schottky-type anomaly originating from the addenda heat capacity very precisely, we have revealed that the low-field specific heat of our sample increases in proportion to $H^{1/2}$ with no multigap structure at 0.06 K. This behavior is in sharp contrast to the previous reports [6], and suggests that multiple gaps on the three bands (α, β, and γ) equivalently survive up to high fields and possess nodes somewhere. In addition, the fourfold oscillation in the specific heat observed under an in-plane rotating field [6] does not change its sign even at a low temperature of $0.04T_c$ in the low-field region (Figs. 1(a) and 1(b)).

The absence of a sign change in the fourfold specific-heat oscillation is incompatible with vertical line node scenario, such as the $d_{x^2-y^2}$- and d_{xy}-wave type; the present results are clearly different from the cases of vertical line node superconductors such as $CeCoIn_5$ [4]. Also, it is obvious that the present observations cannot be explained within the anticipated chiral-*p*-wave scenario. By contrast, the results favorably support the presence of horizontal line nodes; the specific-heat oscillation arises due to nodal quasiparticles that have anisotropic in-plane Fermi velocity of the cylindrical γ band. On the basis of microscopic theoretical calculations, the observed field and temperature variations of the specific-heat oscillation can be reproduced by assuming the presence of horizontal line nodes on cylindrical bands whose Fermi velocity is highly anisotropic within the plane (Fig. 1(c)). The agreement between the experimental and the calculated results becomes even better by taking into account the Pauli-paramagnetic effect. Our findings, in particular the presence of horizontal line nodes in the gap, challenge the historical view of Sr_2RuO_4 and call for reconsideration of its order parameter.

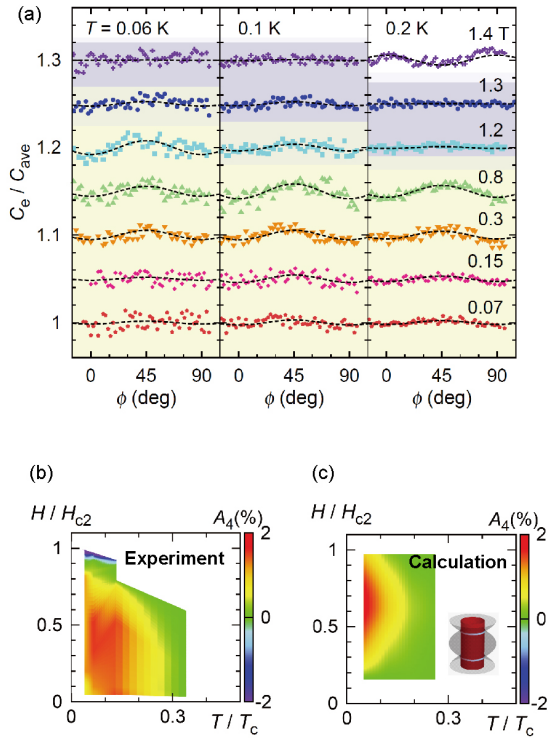

Fig. 1. (a) Field-angle dependence of the specific heat under a rotating magnetic field within the *ab* plane of Sr_2RuO_4. (b) The *H*-*T* phase diagram of the normalized amplitude A_4 of the fourfold specific-heat oscillation. (c) The calculated results of $A_4(T, H)$ obtained by assuming a horizontal line node gap (inset), anisotropic in-plane Fermi velocity, and the Pauli-paramagnetic effect.

References

[1] Y. Maeno, S. Kittaka, T. Nomura, S. Yonezawa, and K. Ishida, J. Phys. Soc. Jpn. **81**, 011009 (2012).
[2] S. Yonezawa, T. Kajikawa, and Y. Maeno, Phys. Rev. Lett. **110**, 077003 (2013).
[3] S. Kittaka *et al.*, Phys. Rev. B **90**, 220502(R) (2014).
[4] T. Sakakibara, S. Kittaka, and K. Machida, Rep. Prog. Phys. **79**, 094002 (2016).
[5] S. Kittaka *et al.*, J. Phys. Soc. Jpn. **87**, 093703 (2018).
[6] K. Deguchi *et al.*, J. Phys. Rev. Lett. **92**, 047002 (2004).

Authors

S. Kittaka, S. Nakamura, T. Sakakibara, N. Kikugawa[a], T. Terashima[a], S. Uji[a,b], D. A. Sokolov[c], A. P. Mackenzie[c], K. Irie[d], Y. Tsutsumi[e,f], K. Suzuki[d], and K. Machida[d]

[a]National Institute for Materials Science
[b]University of Tsukuba
[c]Max Planck Institute for Chemical Physics of Solids
[d]Ritsumeikan University
[e]The University of Tokyo
[f]RIKEN

Construction of Three-Dimensional Anionic Molecular Frameworks Based on Hydrogen-Bonded Metal Dithiolene Complexes and the Crystal Solvent Effect

Mori Group

Metal organic frameworks (MOFs) and covalent organic frameworks (COFs) are a class of crystalline materials with highly periodic structures formed through coordination or covalent bonds. Extensive synthetic studies of these materials have been carried out, because of the uniqueness of their structures and the resulting functionalities, such as gas adsorption/separation, catalytic, and sensing abilities and fuel cell properties. In addition, hydrogen-bonded (H-bonded) organic frameworks (HOFs) have recently emerged as a new class of such crystalline materials. By utilizing H-bonds instead of coordination or covalent bonds, HOFs have generally better crystallinity, solution processability, and flexibility than MOFs and COFs. Such ionic frameworks are expected to show unique features different from conventional neutral ones, due to their intrinsic ionic nature and the accompanying cation–anion interactions. However, the number of ionic frameworks reported so far is limited.

Recently, we have designed and synthesized a novel metal dithiolene complex with hydrogen-bonding (H-bonding) ability, $[Au(catdt)_2]^-$ (catdt: catechol-4,5-dithiolate) and successfully constructed $[Au(catdt)_2]^-$-based three dimensional (3D) anionic molecular frameworks in two kinds of salts, $(Ph_4P)[Au(catdt)_2]\cdot 0.5H_2O$ (**1a**) and $(Ph_4P)[Au(catdt)_2]\cdot Et_2O\cdot n(solv)$ (**1b**; solv = Et_2O and/or acetone). To our knowledge, these are the first examples of the 3D molecular frameworks based on H-bonded metal dithiolene complexes. Importantly, these frameworks are constructed through 3D intermolecular H-bonds between $[Au(catdt)_2]^-$ molecules, and have tubular channels occupied by large Ph_4P^+ cations, where multiple cation–anion short contacts are formed to stabilize the 3D framework structures. Furthermore, in addition to **1a** and **1b** with 3D frameworks, we have obtained $(Ph_4P)[Au(catdt)_2]\cdot 2THF$ (**1c**) having a 2D layered structure. A detailed comparison of the structures of these compounds reveals that the included solvent molecules play an important role in regulating the intermolecular interactions and assembled structures. Interestingly, we have found that, due to the differences in the H-bonding ability and molecular size of H_2O and Et_2O, the wall structures of the 3D frameworks in **1a** without voids and **1b** with voids are qualitatively different. [1]

Three kinds of 1:1 salts of Ph_4P^+ and $[Au(catdt)_2]^-$, that is, $(Ph_4P)[Au(catdt)_2]\cdot 0.5H_2O$ (**1a**), $(Ph_4P)[Au(catdt)_2]\cdot Et_2O\cdot n(solv)$ (**1b**; solv = Et_2O and/or acetone), and $(Ph_4P)[Au(catdt)_2]\cdot 2THF$ (**1c**), were synthesized, and their structures and chemical compositions were determined by single crystal X-ray analysis. Recrystallization of the obtained powder from acetone/hexane, acetone/Et_2O or THF/hexane provided the salt **1a** (containing H_2O) as yellowish brown needle-like crystals, **1b** (containing Et_2O and/or acetone) as yellow plate-like crystals or **1c** (containing THF) as green plate-like crystals, respectively.

We first compare the structures of three kinds of novel $[Au(catdt)_2]^-$-based salts, $(Ph_4P)[Au(catdt)_2]\cdot 0.5H_2O$ **1a**, $(Ph_4P)[Au(catdt)_2]\cdot Et_2O\cdot n(solv)$ (**1b**; solv = Et_2O and/or acetone), and $(Ph_4P)[Au(catdt)_2]\cdot 2THF$ (**1c**). All of them are 1:1 salts of Ph_4P^+ and $[Au(catdt)_2]^-$; however, their crystal structures are qualitatively different from each other,

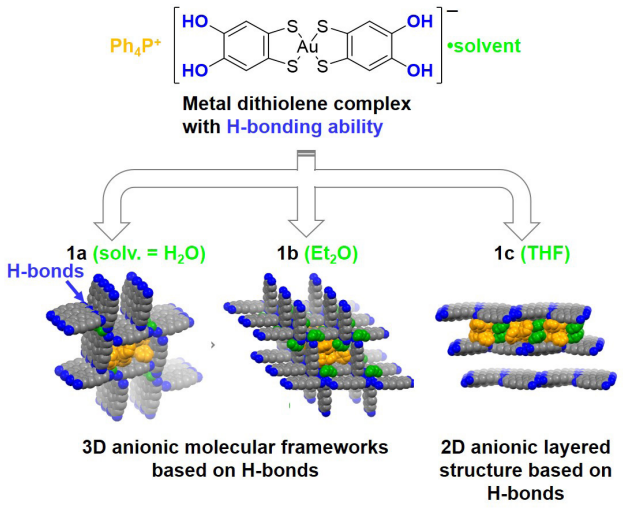

Fig. 1. On the basis of the design and synthesis of an anionic gold dithiolene complex $[Au(catdt)_2]^-$ with four hydroxyl groups, we have successfully constructed the first 3D molecular frameworks based on H-bonded metal dithiolene complexes, $(Ph_4P)[Au(catdt)_2]\cdot 0.5H_2O$ (**1a**) and $(Ph_4P)[Au(catdt)_2]\cdot Et_2O\cdot n(solv)$ (**1b**; solv = Et_2O and/or acetone) as well as 2D layered structure of $(Ph_4P)[Au(catdt)_2]\cdot 2THF$ (**1c**). The key for constructing the 3D frameworks are (i) connecting the planar $[Au(catdt)_2]^-$ molecules with 3D intermolecular H-bonds and (ii) introducing large Ph_4P^+ cations into the channels. Interestingly, metal complexes are highly influenced by the solvent molecules included in the crystals (especially, the molecular size and shape and H-bonding abilities), which leads to variations in the assembled structure of the $[Au(catdt)_2]^-$ molecules; namely, a 3D framework with densely packed walls in water containing **1a**, a 3D framework with loosely packed walls in ether-containing **1b**, and a 2D layered structure in THF containing **1c**.

depending on the solvent molecules included in the crystal. The most prominent difference is the dimensionality of the assembled structures of $[Au(catdt)_2]^-$; namely, in the water and ether-containing salts **1a** and **1b**, this planar anionic molecule forms a 3D assembled structure (i.e., 3D framework, Fig. 1), whereas in the THF-containing salt **1c**, it forms not a 3D but a 2D structure (i.e., 2D layers). Furthermore, although both the 3D framework structures in **1a** and **1b** have tubular channels with a similar size, the structures of their walls are significantly different from each other; namely, the walls in **1a** are densely packed with $[Au(catdt)_2]^-$, whereas those in **1b** are loosely packed to form voids, into which the cation and Et_2O molecules partially penetrate (Fig. 1). These differences should be caused by changing the intermolecular interactions between the component molecules upon the change of the crystal solvent.

We finally discuss how the crystal solvent makes differences in the intermolecular interactions and assembled structures. Here, we focus on the H-bonding ability, size, and shape of the crystal solvents. Et_2O, included in the 3D system **1b**, and THF, included in the 2D system **1c**, have proton- accepting ability due to the ether oxygen atom, which actually allows them to form the H-bonds with the catechol O–H protons of $[Au(catdt)_2]^-$ molecules. On the other hand, the overall shapes of these solvent molecules are greatly different from each other [rod-shaped (Et_2O) vs. disk-shaped (THF)], which should contribute to the great structural difference in **1b** and **1c** (i.e., 3D vs. 2D). Namely, due to the disk shape, the THF molecules are positionally (orientationally) disordered, which leads to the formation of the THF–THF H-bonds and consequently the 2D layered structure. In contrast, the rod-shaped Et_2O molecules have no such structural disorder and additional intermolecular interactions; thus they seem to simply occupy the space

between the large Ph_4P^+ and $[Au(catdt)_2]^-$ molecules without interrupting the intermolecular interactions between the Ph_4P^+ and $[Au(catdt)_2]^-$ molecules for constructing the 3D framework. Meanwhile, due to the steric bulkiness of the ethyl groups in Et_2O, the walls of the 3D framework have the voids. In contrast, the water containing 3D system **1a** has no such voids and thus the wall is densely packed with the lateral S···S interactions between $[Au(catdt)_2]^-$ molecules. This is probably because the solvent water molecules are involved in the wall structure, which should eliminate the above mentioned steric hindrance effect from the solvent molecules. Here, the water molecule has both proton-donating and -accepting abilities, in contrast to Et_2O and THF having only proton-accepting ability. In addition, the size of water molecule is much smaller than that of the others. These features should allow the water molecules to exist between the catechol moieties of $[Au(catdt)_2]^-$ molecules and participate in the densely packed wall structure of the 3D framework. Therefore, we have successfully illustrated the role and effect of the crystal solvent molecules on the construction of these new 3D anionic molecular frameworks based on $[Au(catdt)_2]^-$ in terms of the molecular size and shape and H-bonding abilities. As for the next step, by taking advantage of this new type of metal dithiolene complex with H-bonding abilities, we are currently investigating cooperative properties and functionalities of H-bond dynamics (e.g. dielectric properties and proton conductivity) and π–/d-electrons (e.g. electronic conductivity and magnetic properties).

Reference

[1] S. Yokomori, A. Ueda, T. Higashino, R. Kumai, Y. Murakami, and H. Mori, CrystEngCommun, **21**, 2940 (2019).

Authors

S. Yokomori, A. Ueda, T. Higashino, R. Kumai[a], Y. Murakami[a], and H. Mori

[a]Condensed Matter Research Center (CMRC) and Photon Factory, Institute of Materials Structure Science, High Energy Accelerator Research Organization (KEK)

Quantum Size Effects Associated with Ultra-Thinning of Layered Semimetals

Osada Group

We have investigated thickness dependence of the electronic properties of two layered semimetals, graphite and WTe_2, under magnetic fields. Their monolayer limits are known as a 2D Dirac fermion system (graphene) and a 2D quantum spin Hall insulator, respectively. Therefore, it is significant to see how their electronic properties changes associated with thinning them.

Generally, under the normal magnetic field, the band structure of the layered conductor is quantized to a set of Landau subbands with interlayer dispersion. Here, as the sample thickness approaches the de Broglie wavelength, the interlayer electron wave number is quantized, so that the bulk Landau subbands separates to discrete levels as shown in Fig. 1. This causes various size effects on electronic properties.

Bulk graphite shows a unique field-induced electronic phase transition above 30 T. Although the density wave formation due to the $2k_F$ instability of the Landau subband was proposed as a possible mechanism of the transition,

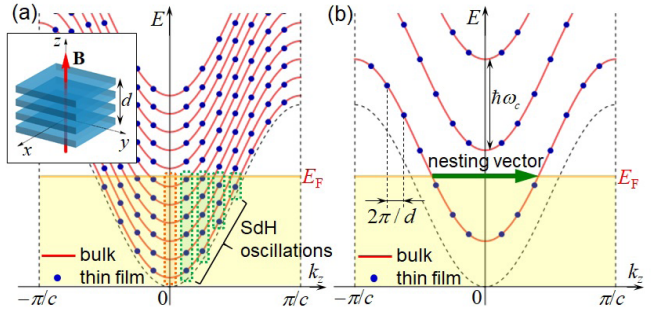

Fig. 1. Concept of the quantum size effect under magnetic fields. The Landau subbands in the bulk (red curves) are quantized into discrete levels (blue circles) due to the size effect in thin films. (a) In the low field region, several SdH oscillations with different frequencies appear in thin films, instead of the oscillation of the extremal orbit in the bulk. (b) At the high-field quantum limit, the field-induced density wave transition due to the $2k_F$ instability of the lowest subband is suppressed by the discretization of the subband.

it has never been confirmed yet. In order to identify the high field phase, we performed transport measurements of thin-film graphite samples under the magnetic field up to 40 T, which was generated by a home-made miniature pulse magnet system. The thin-film flake was prepared on a silicon substrate by the mechanical exfoliation technique, and the device structure was fabricated using the electron beam lithography (Fig. 2(b)). As seen in Fig. 2(a), the magnetoresistance shows a saturation around 10 T, above which there exist only a few occupied Landau subbands (quasi-quantum limit). The field-induced phase transition appears above 30 T as indicated by an arrow. On the phase diagram, the phase boundaries in thin films shift to higher fields, accompanied by a reduction in temperature dependence. These results are consistently explained by the density wave model with the quantum size effect, because the $2k_F$ instability of the Landau subband is weakened by the discretization of the subband in thin films (Fig. 1(b)). The present finding strongly suggests the density wave state standing along the interlayer direction [1].

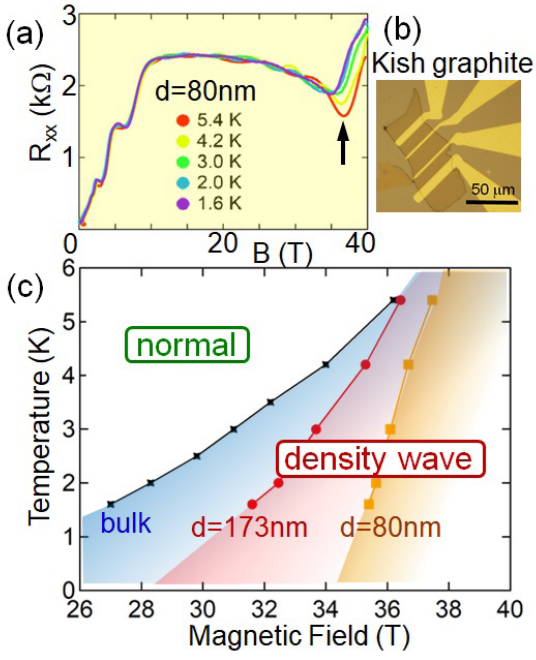

Fig. 2. Quantum size effect on the field-induced electronic phase transition in graphite. (a) Transverse magnetoresistance of a graphite thin film with the thickness of 80 nm. The arrow indicates the field-induced transition. (b) Microscope image of a Kish graphite thin film device. (c) Phase diagram of the field-induced transition in graphite thin films.

The bulk crystal of a layered transition metal dichalcogenide compound, 1T'-WTe_2, is known as a 3D type-II Weyl semimetal. In order to see the change of topological states, we carried out the magnetotransport measurement of WTe_2 thin films with reducing their thickness. Since WTe_2 is degraded in the atmosphere, the mechanical exfoliation process was performed in the grove box. The clear Shubnikov-de Haas (SdH) oscillations are observed on positive magnetoresistance. The FFT spectrum of the SdH oscillations has mainly four peaks, which correspond to the extremal orbits surrounding four Fermi surfaces of the bulk. Their peak frequencies start to decrease with a film thickness of about 50 nm or less. Moreover, as the film thickness decreases, many weak subpeaks appear on the low frequency side of each main peak below about 30 nm. According to the picture of the quantum size effect (Fig. 1(a)), the observed subsidiary SdH oscillations with different frequencies originate from the 2D subbands, to which the bulk band with a Fermi surface is quantized.

Reference

[1] T. Taen, K. Uchida, and T. Osada, Phys. Rev. B **97**, 115122 (2018).

Authors

T. Osada, T. Taen, H. Adachi, T. Uchida, and K. Uchida

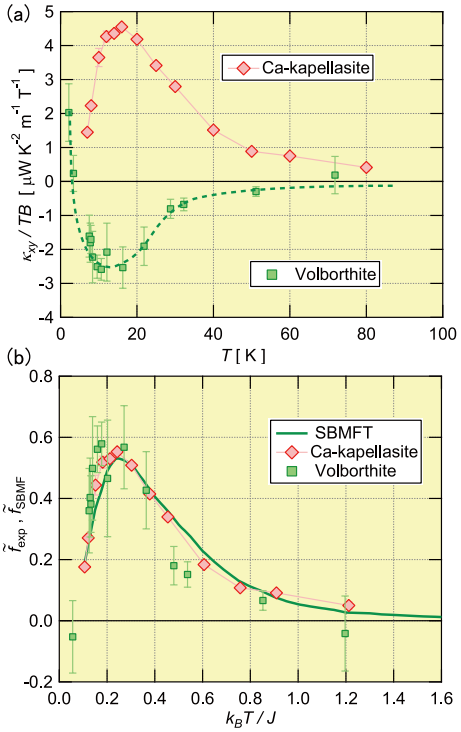

Fig. 2. (a) The temperature dependence of the thermal Hall conductivity divided by the temperature and the magnetic field (κ_{xy}/TB) of Ca-kapellasite [1] and volborthite [4]. (b) Normalized thermal Hall conductivity of these two compounds ($\tilde{f}_{exp}$, symbols) and that of Schwinger-boson mean field theory ($\tilde{f}_{SBMF}$, solid line) show a remarkable agreement by tuning J and D as fitting parameters. The values of parameters (J/k_B, D/J) used for the fittings are (66, 0.12) and (60, -0.07) for Ca kapellasite and volborthite, respectively.

Spin Thermal Hall Conductivity in a Kagomé Antiferromagnet

Yamashita and Kawashima Groups

Searching for the ground state of a kagomé Heisenberg antiferromagnet (KHA) has been one of the central issues of condensed-matter physics, because the KHA is expected to host spin-liquid phases with exotic elementary excitations.

To study the elementary excitations, we investigate the longitudinal (κ_{xx}) and transverse (κ_{xy}) thermal conductivities of a new candidate of S = 1/2 KHA Ca kapellasite ($CaCu_3(OH)_6Cl_2{\cdot}0.6H_2O$) [1]. The magnetic Cu^{2+} ions in Ca kapellasite form an ideal kagomé structure (Fig. 1 (a) and (b)). The fitting of the temperature dependence of the magnetic susceptibility shows that the spin Hamiltonian in Ca kapellasite is well approximated as an ideal KHA with the effective spin interaction energy J/k_B ~ 66 K [1, 2]. Although the ground state is not a quantum spin liquid, the magnetic transition temperature T^*~ 7 K is much lower than J/k_B, providing a wide temperature range of the spin liquid phase $T^* < T < J/k_B$ to study the elementary excitations.

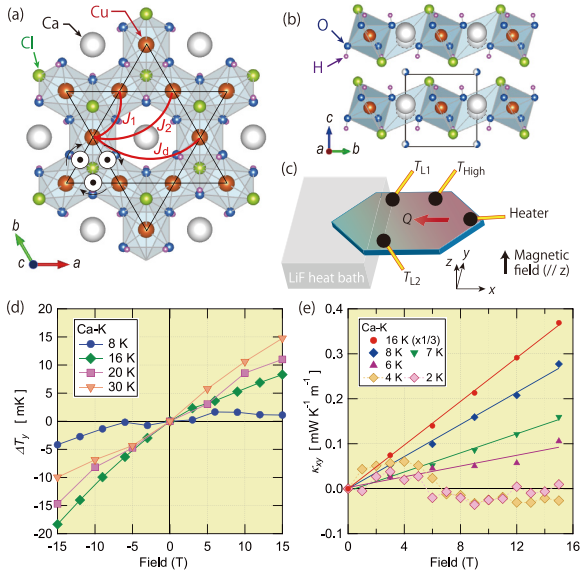

Fig. 1. (a, b) Crystal structure of Ca kapellasite viewed along the c axis (a) and the a axis (b). The direction of the Dzyaloshinskii-Moriya interaction (D) is shown by the ⊙ symbols. J_1, J_2, and J_d (solid red lines) represent the nearest-neighbor, next nearest-neighbor, and diagonal magnetic interactions, respectively [2]. (c) An illustration of our experimental setup. Three thermometers (T_{High}, T_{L1}, T_{L2}) and a heater were attached to the sample. A heat current $Q \parallel x$ was applied within the ab plane and a magnetic field was applied along the $c \parallel z$ axis. (d, e) The field dependence of the transverse temperature difference $\Delta T_y \equiv T_{L1} - T_{L2}$ (d) and κ_{xy} (e). Solid lines in (e) represent linear fits.

Figure 1 (d) shows the field dependence of the transverse temperature difference $\Delta T_y \equiv T_{L1} - T_{L2}$ (see Fig. 1 (c) for the experimental configuration). Remarkably, asymmetric field dependence is clearly observed, demonstrating a thermal Hall signal in this transparent insulator. By asymmetrizing ΔT_y with respect to the field direction, we obtain the field dependence of κ_{xy} (Fig. 1 (e)) which is found to be linear to the field in the spin liquid phase.

The temperature dependence of κ_{xy}/T shows an increase as lowering temperature below J/k_B, which is followed by a peak at $T \sim J/3k_B$ (Fig. 2 (a)). Quite unexpectedly, the temperature dependence and the magnitude of κ_{xy} of Ca kapellasite is similar to that of another kagomé antiferromagnet volborthite [4], whereas the κ_{xx} in Ca kapellasite is about one order of magnitude smaller than that of volborthite. Given that κ_{xx} is dominated by phonons in this temperature range, similar $|\kappa_{xy}|$ in these kagomé compounds rules out phonons as the origin of κ_{xy}.

We find that κ_{xy} is well reproduced, both qualitatively and quantitatively, by spin excitations described by the Schwinger-boson mean-field theory [3] with the Dzyaloshin-

skii-Moriya interaction of D. Most remarkably, both κ_{xy} of Ca kapellasite and that of volborthite are found to converge to one single curve of our Schwinger-boson calculation only by choosing J and D as fitting parameters (Fig. 2 (b)). This excellent agreement demonstrates not only that the thermal Hall effect in these kagomé antiferromagnets is caused by spins in the spin liquid phase, but also that the elementary excitations of this spin liquid phase are well described by the bosonic spinons. Although whether our ansatz is the only successful state for describing κ_{xy} or other spin liquid states – in particular spin liquids with fermionic spinons having a different κ_{xy} – remains an open question, our results suggest that thermal Hall conductivity of a kagomé antiferromagnet has a common temperature dependence described by Schwinger bosons.

References

[1] H. Doki, M. Akazawa, H.-Y. Lee, J. H. Han, K. Sugii, M. Shimozawa, N. Kawashima, M. Oda, H. Yoshida, and M. Yamashita, Phys. Rev. Lett. **121**, 097203 (2018).
[2] H. Yoshida *et al.*, J. Phys. Soc. Jpn. **86**, 033704 (2017).
[3] H. Lee, J. H. Han, and P. A. Lee, Phys. Rev. B **91**, 125413 (2015).
[4] D. Watanabe *et al.*, Proc. Natl. Acad. Sci. USA **113**, 8653 (2016).

Authors

M. Yamashita and N. Kawashima

Floquet-Theoretical Formulation and Analysis of High-Harmonic Generation in Solids

Tsunetsugu Group

High-harmonic generation (HHG) is a nonlinear optical phenomenon, and monochromatic input light irradiates a target medium to be converted to output with multiple high harmonics, which is an indispensable technology for the state-of-the-art ultrafast physical measurements. While atomic gases were traditionally used target media, recent experiments have achieved the high-harmonic generation in bulk solids [1]. However, it remains an open problem how the interaction of light with electrons in solids results in the conversion to higher frequencies.

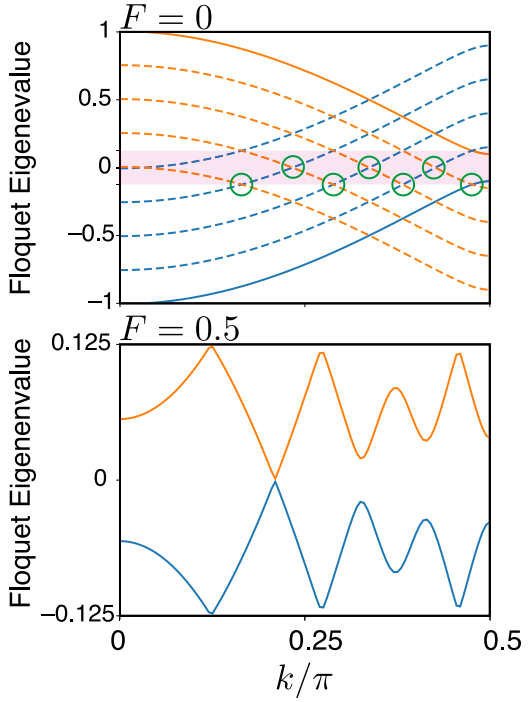

Fig. 1. Energy dispersion of Floquet bands in two cases with different electron-light coupling $F \propto \Omega^{-1}E$ (electric field amplitude of input light): (upper) no coupling and (lower) non-zero coupling. Dimensionless frequency of input light is $\Omega = 0.25$. The non-zero coupling F avoids crossings of replicas of the two original energy bands (solid lines in the upper panel).

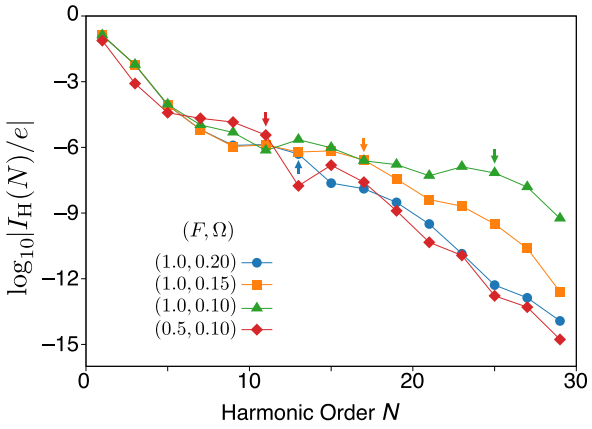

Fig. 2. High-harmonic spectrum of electric current shown in logarithmic scale. The cutoff order $N_{\max}$ represented by the arrow is proportional to $F/\Omega \propto E/\Omega^2$.

In this study [2], we invoke the mathematical tool known as Floquet's theorem to analyze the electron dynamics driven by light with single frequency Ω, which induces HHG in output light. We have tailored this theoretical framework for a simple lattice electron model in one dimension. This model is a tight-binding Hamiltonian with two bands which are controlled by site-alternating potentials, and electrons acquire a time-oscillating phase in their hopping amplitude due to their coupling to input light. We have obtained an analytical solution for the time evolution of electron wave function in the limit of no potential scattering, and proceed to analyze the effects of the potential scattering by a perturbation approach. While the highest frequency of HHG in the no-scattering limit is too low to explain the related experimental data, we have found that it becomes large enough as the scattering amplitude increases.

Our result [2] also predicts that the highest order in HHG is inversely proportional to the square of the input frequency, $N_{\max} \propto \Omega^{-2}$, in contrast to the conventional scaling $\propto \Omega^{-1}$ in atomic gases. This anomalous behavior deserves experimental confirmation. Besides, our Floquet-theoretical approach is general and thus applicable to various lattice systems. Therefore, for realizing effective HHG, it is useful to employ this approach and examine the effects of important characteristics of the model, such as dimensionality and symmetry of solids.

References

[1] S. Ghimire *et al.*, Nat. Phys. **7**, 138 (2011).
[2] T. N. Ikeda, K. Chinzei, and H. Tsunetsugu, Phys. Rev. A **98**, 063426 (2018).

Authors

T. N. Ikeda and H. Tsunetsugu

Heat Transport via a Two-State System

Kato Group

Heat transport in macroscopic systems has been studied for long time. Recent technological progress has enabled us to measure heat transport carried by photons or phonons via a nanoscale object, for which quantum properties of the system are revealed [1]. Based on this development, we studied heat transport in the spin-boson model, in which a two-state system is coupled to two thermal reservoirs (see Fig. 1 (a)) [2]. Even though this spin-boson model is simple, it is known that there appear various physical phenomena such as the Kondo effect [3,4].

The properties of the thermal reservoirs are characterized by a spectral density function, $I(\omega) \propto \omega^s$. In Ref. [2], we studied thermal conductance for heat transport via a two-state system for arbitrary exponent s, comparing analytic approximations with numerical results based on the continuous-time quantum Monte Carlo method. By systematic comparison, we revealed that heat transport via a two-state system is described by one of three processes, i.e., (i) sequential tunneling, (ii) co-tunneling, and (iii) incoherent tunneling (see Fig. 1 (b)-(d)). We derived an asymptotically exact expression for the sufficiently low-temperature region (the co-tunneling regime). This formula predicts power-law temperature dependence at low temperatures. We also found that for the high-temperature or strong-coupling regions (the incoherent tunneling regime), the thermal conductance is well explained by the noninteracting-blip approximation (NIBA).

As an example, we show the temperature dependence of the thermal conductance for the ohmic reservoir ($s = 1$) and $\alpha = 0.1$ (α is a dimensionless system-reservoir coupling constant) in Fig. 2. At low temperatures, the numerical result (the legends) agrees well with the asymptotically exact formula for the cotunneling process (the blue dashed line). In this regime, the thermal conductance is always proportional to $T^3 (= T^{2s+1})$, which is consistent with the result of Ref. [4]. At moderate temperatures and high temperatures, the numerical result deviates from the cotunneling formula, and instead agrees well with the NIBA (the black solid line). We note that the thermal conductance obtained by the NIBA is proportional to $T^{3-\alpha}$ at low temperatures as indicated in the figure, and deviates from the low-temperature numerical results. We also show the approximate formula for the sequential tunneling (the green dot-dashed line), and the

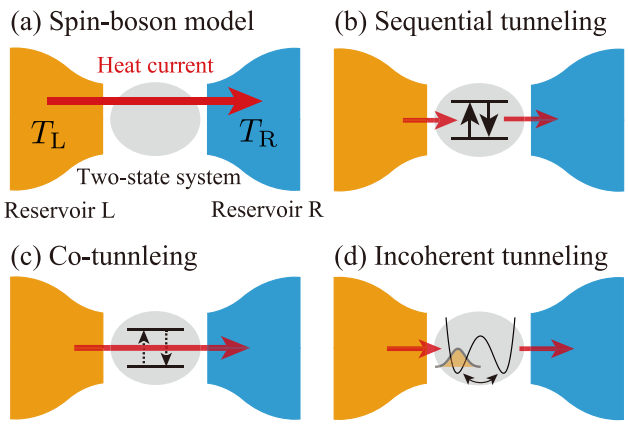

Fig. 1. (a) A schematic of the system considered in the present study. Heat transport is governed by one of three processes; (b) sequential tunneling process, (c) co-tunneling process, and (d) incoherent tunneling process.

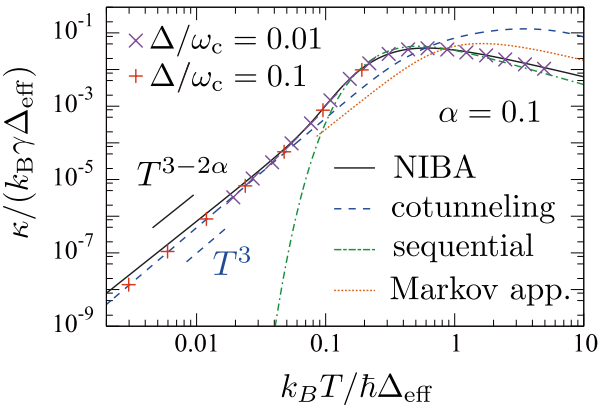

Fig. 2. Temperature dependence of the thermal conductance for the ohmic case ($s = 1$).

Markov approximation for the incoherent tunneling (the orange dotted line). The former agrees with numerical data at moderate temperatures, while the latter clearly deviates from the numerical results, indicating the importance of the non-Markov properties of the system.

Our study will provide a useful basis for deep understanding of heat transport via nanoscale devices, and as well a platform for experiments attempting to access many-body effect in heat transport of mesoscopic devices.

References

[1] A. Ronzani *et al.*, Nat. Phys. **14**, 991 (2018).
[2] T. Yamamoto, M. Kato, T. Kato, and K. Saito, New J. Phys. **20**, 093014 (2018).
[3] A. J. Leggett *et al.*, Rev. Mod. Phys. **59**, 1 (1987).
[4] K. Saito and T. Kato, Phys. Rev. Lett. **111**, 214301 (2013).

Authors
T. Yamamoto and T. Kato

Realization of a Current-Controlled Superconducting Device

Katsumoto Group

Ultra-high speed, low-power consumption logic device action has been predicted for Josephson superconducting junctions, which dream, however, has not come true yet for more than three decades. The device action itself had been confirmed at the beginning of the 1980s [1]. Nevertheless,

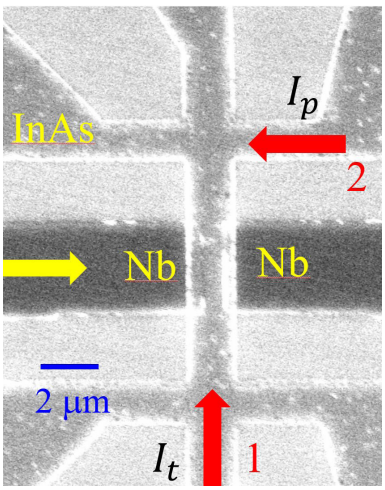

Fig. 1. Scanning electron micrograph of the sample. The yellow arrow indicates the supercurrent while two red arrows indicated the transverse (no.1) and the parallel (no.2) normal currents, respectively.

the two-terminal nature of the junction has blocked the application to the real world of logic devices. The obstacle is explained as follows. The switching to normal state occurs when the junction is "fired" by applying a bias current larger than the critical current J_c (J_{c1}). Then to switch the next junction a current larger than its J_c (J_{c2}) is required while the current swing of the first junction is J_{c1}. Hence for the circuit action, condition $J_{c1} > J_{c2}$ should be fulfilled. The condition means that J_c decreases monotonically over the chain of logic gates, thus sharply limits the scalability of the circuit. The finding of a gate-controllable supercurrent through the two-dimensional electrons (2DE) on the surfaces of InAs [2], this was thought to solve the problem. However, as a voltage-driven device, the Josephson junctions have too high off-conductance, and the obstacle was realized to exist stubbornly. Therefore a current-current three(or four)-terminal device is required for the practical use.

We here report pure current-control of supercurrent, which would solve the long-standing technical problem. We prepared a 2DE in an InAs quantum well grown on an InP substrate. Figure 1 shows the sample structure, in the center of which a Nb-InAs 2DE-Nb superconducting junction is formed. Besides, the sample has six normal terminals, through which local or non-local electric currents can flow. InAs 2DE is known to have a strong Rashba-type spin-orbit interaction (RSOI), and the layered structure is design to maximize the RSOI.

One of the expected device actions is described as follows. When a supercurrent is flowing between the two Nb electrodes, a normal current is applied transverse to the supercurrent. The normal current is associated with the spin Hall effect, which causes spin accumulation at the super-normal interfaces and breaks the time-reversal symmetry locally. The normal current can thus reduce the critical current of the superconducting junction. The other is a kind of "remote reduction," in which the normal current is applied parallel to the supercurrent but at a different part of the sample (red arrow no.2). In this case, the normal current causes the spin current, which should have a significant disorder in electron spins through the Zitterbewegung [3] and crosses the supercurrent. The disordered spin current again should lead to the reduction of the critical current.

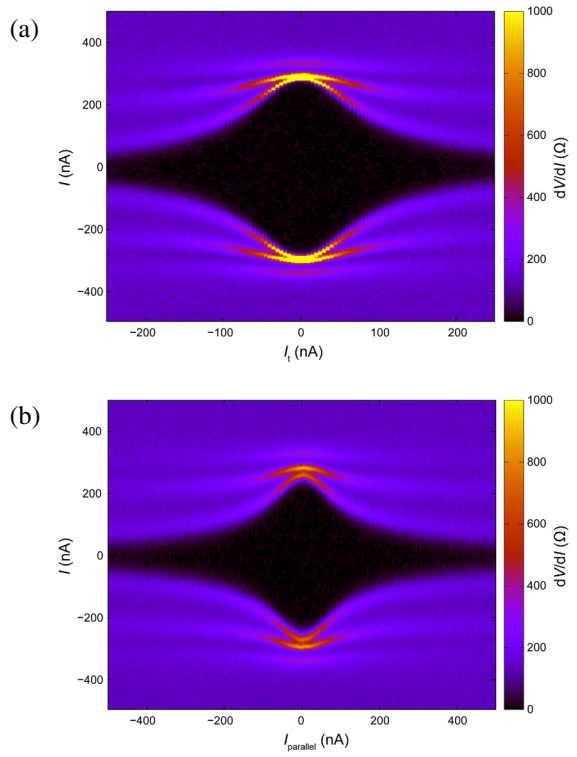

Fig. 2. (a) Color plot of the junction resistance versus the plane of transverse current and junction current. The black region corresponds to the zero-resistance state. (b) The same for the parallel current.

In the experiments, the care was taken to avoid heating by the normal currents and the application of voltages due to the imbalance of the potentials at the normal electrodes. Figure 2(a) is a color plot of the resistance of the superconducting junction against the junction current and the control current. The black region corresponds to the zero-resistance state, and an apparent reduction of the critical current is observed. The current gain (the derivative of the edge line on the zero-resistance region) is larger than unity (0 dB) below 100 nA of the transverse current. The result of the remote-reduction experiment is shown in Fig. 2(b). The remote current also reduces the critical current through the sensitivity is lower, and the region for positive current gain (above 0 dB) is limited to just around the zero parallel currents.

In conclusion, we have realized a current-controlled four terminal superconducting device with finite current gains.

References
[1] T. R. Gheewala, IEEE Trans. Electron Devices **27**, 1857 (1980).
[2] H. Takayanagi and T. Kawakami, Phys. Rev. Lett. **54**, 2449 (1985).
[3] Y. Iwasaki, Y. Hashimoto, T. Nakamura, and S. Katsumoto, Sci. Rep. **7**, 7909 (2017).

Authors
T. Nakamura, Y. Hashimoto and S. Katsumoto

Magneto-Thermodynamic Properties in Submicron Wires of Pd-doped FeRh

Otani Group

An FeRh alloy with B2 order shows a first-order phase transition from antiferromagnetic (AFM) to ferromagnetic (FM) phases with raising temperature. As the transition temperature is tunable around room temperature, this is a candidate material for several applications such as heat-assisted magnetic recording, AFM memories and memristor devices. Recently, an asymmetric behavior around the AFM-FM phase transition has been reported on some tiny sample structures. Remarkably, a discontinuous and asymmetric resistance change around the phase transition was reported in submicron wires of FeRh, which is caused by suppression of the nucleation of AFM domains during the cooling process [1]. In this work, we performed resistivity measurements of submicron wires of Pd-doped FeRh as a function of temperature and external magnetic field. We further evaluated some thermal properties such as an energy loss around the temperature hysteresis in each wire to characterize those finite-size effect.

We used Pd-doped FeRh alloy in order to decrease the AFM-FM phase transition temperature. A 60-nm-thick epitaxial film of Pd-doped FeRh was prepared and fabricated into submicron wires. Detailed processes for film growth and patterning are shown in Ref. 2. As the resistivity in AFM phase is larger than that in FM phase, the electrical transport measurement can be a probe to detect the AFM-FM phase transition which is induced by sweeping temperature or external magnetic field. The resistance on 270-nm-wide wire against temperature and magnetic field is plotted in Fig. 1(a). We can see the temperature-driven and field-driven hysteresis

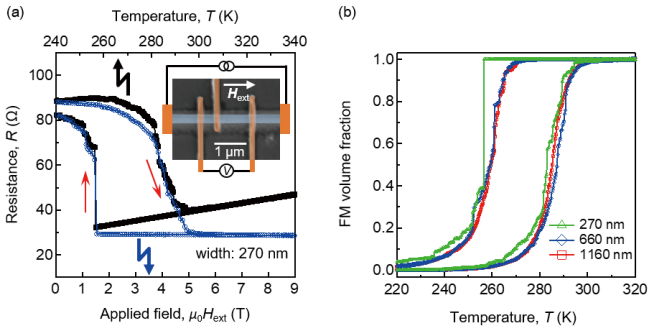

Fig. 1. Hysteresis loops due to AFM-FM transition on submicron wires of Pd-doped FeRh [2]. (a) Resistance measurements on 270-nm-wide wire of Pd-doped FeRh against temperature (black) and in-plane magnetic field (blue). The temperature-driven hysteresis loop was measured without applying a magnetic field and the field-driven one was done at a constant temperature of 240.0 K. Inset is a SEM image of the wire. (b) Volume fraction of ferromagnetic phase against temperature which were estimated from resistance of the submicron wires.

loops due to the AFM-FM phase transition. Though the resistance contains small jumps under the transition to FM phase, it showed a large discontinuous change on the opposite arm, the transition to AFM phase. These asymmetries and step-like structures in both hysteresis loops would indicate the nucleation processes of AFM and FM domains are confined by the sample size, which is also reported in Ref. 1. We further investigated how the hysteric behavior changes by the size of wires. We prepared 270nm-, 660-nm- and 1160-nm-wide wires by the same method and measured their resistances with sweeping temperature. Under an assumption that all magnetic domains are aligned along the longitudinal direction of the wire, the volume fraction of FM domains can be calculated from the measured resistance in each wire as shown in Fig. 1(b). We can find the enhanced asymmetry in narrow wires. To evaluate this finite-size effect in wires, we estimated the energy loss around the phase transition from simple thermodynamic equations. We found the energy losses around the hysteresis loops are larger in narrower wires. Also, all wires showed larger losses than the unpatterned film. These results would suggest that the finite-size effect, probably a restriction in magnetic domain structures across the phase transition, appears in a macroscopic energy loss. This method can be a probe to characterize the rectified domain nucleation process in tiny volume samples by simple electrical measurements.

References
[1] V. Uhlír *et al*., Nature Commun. **7**, 013113 (2016).
[2] K. Matsumoto *et al*., IEEE Trans. Magn. **54**, 2300904 (2018).

Authors
Y. Otani and K. Matsumoto

Dynamic Interface Formation in Magnetic Thin Film Heterostructures

Komori Group

In magnetic thin film heterostructures, interaction at the interface plays a dominant role in the development of novel electronic and magnetic properties. The interlayer coupling strength primarily relies on the interfacial structure at the atomic scale, including atomic roughness, steps, and intermixing. However, the impact of the atomic scale interfacial structure on the magnetic coupling in magnetic thin film

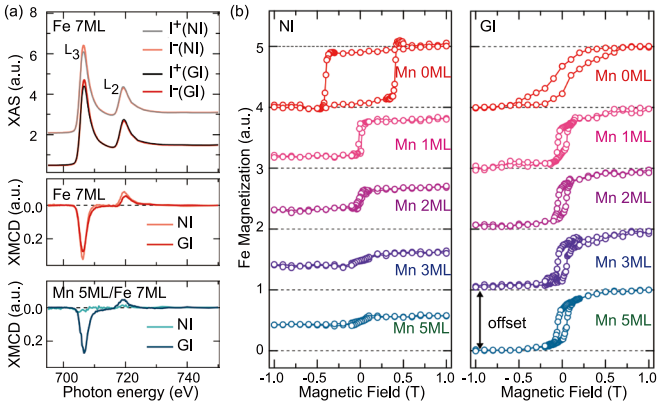

Fig. 1. (a) Fe $L_{2,3}$ remanent XAS (upper) and XMCD (middle) of a 7-ML Fe film on Cu(001), and XMCD (lower) of a 5-ML Mn/7-ML Fe film in the normal incidence (NI) and grazing incidence (GI) geometries. Here, external magnetic field is parallel to the incident x-ray. (b) Iron magnetization curves in the heterostructures of Mn (x ML, x = 0, 1, 2, 3, and 5) overlayers on the 7-ML Fe film measured in the NI (left) and GI (right) geometries. The L_3 XAS peak intensity normalized by the L_2 one is plotted as a function of the magnetic field. In the GI geometry, the magnetic field is applied along the [100] direction of the Cu(001) substrate.

heterostructures has not yet been elucidated well in relation to the macroscopic magnetic properties. We use scanning tunneling microscopy (STM) and x-ray absorption spectroscopy/x-ray magnetic circular dichroism (XAS/XMCD) as complementary tools for clarifying the correlation between the atomic structure at the interface and the magnetism. Successive atomically-resolved STM characterizations of not only structural but also electronic and magnetic properties during the growth of magnetic thin film heterostructures provide crucial information on the atomic-scale interfacial factors in the dynamical process of the interface formation. The element-specific, quantitative and macroscopic observations of electronic and magnetic properties by XAS/XMCD can be linked with the microscopic interface characteristics.

We have studied fcc Fe thin films grown on Cu(001) with Mn overlayers (Mn/Fe films) as a unique system for investigating the interface interaction. [1] The electronic

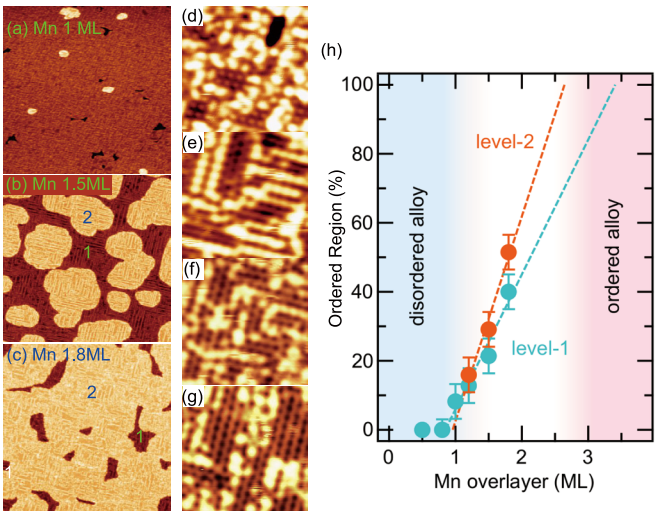

Fig. 2. (a-c) STM images of 7-ML Fe films with 1.0-ML (a), 1.5-ML (b), 1.8-ML (c) Mn overlayers. (d-g) High-resolution surface STM images of 1.0-ML (d), 1.5-ML (e), 1.8-ML films (first (level-1) (f) and second (level-2) (g) levels,). The disorder alloy can be seen in each image as bright protrusions. (h) Statistical plots of the fraction of the ordered alloy region with the (4 × 2) and (4 × 4) reconstructions in level-1 and level-2 as a function of the average thickness of the Mn overlayer. The dashed lines are linear extrapolations of the fractions of the ordered alloy.

and magnetic properties of ferromagnetically-coupled top two layers in the fcc Fe thin film on Cu (001) [2] is susceptible to the structural changes on the atomic scale. At the interface, a collinear and homogeneous antiferromagnetic/ferromagnetic coupling is expected at the Mn/Fe interface as observed in the reference system of Mn thin films on the bulk bcc Fe(001) substrate. Thus, the fcc Fe thin film highlights the role of atomic-scale interfacial factors with the Mn overlayers.

The films were fabricated by successive deposition of Fe and Mn on Cu(001) at room temperature (RT) in an ultrahigh vacuum. The thickness of the fcc Fe layer was fixed to ~ 7 monolayer (ML). The Fe layer in the Mn/Fe film exhibits a two-step spin reorientation transition (SRT) from out-of-plane to in-plane direction with increasing the thickness of the Mn overlayer as observed by XAS/XMCD measurements shown in Fig. 1. After 1 ML deposition of Mn, the coercive field in the magnetic field perpendicular to the film decreases to a value less than that in the in-plain magnetic field. Furthermore, the in-plane anisotropy gradually increases up to 3-ML Mn deposition. Corresponding atomically-resolved STM observations reveal the dynamic structure change from a disordered surface to an ordered one by the Mn deposition at RT as in Fig. 2. First, a disordered surface alloy with the Fe film is formed by the Mn deposition, which induces the first SRT. The ordered-alloy area of the surface gradually increases with increasing the amount of the deposited Mn atoms more than 1 ML on average. The ordering of the alloy completes around 3-ML Mn deposition, which corresponds to the completion of the second SRT.

The present complementary approach by XAS/XMCD and STM successfully disentangles the hidden functionality of the interface alloying, which changes and enhances the magnetic anisotropy in the Fe layer. The results will pave new ways to understand novel phenomena emerging at the interface on the atomic scale, and to improve the electronic and magnetic properties of the magnetic thin film heterostructure.

References

[1] S. Nakashima *et al.*, Adv. Func. Matter. **29**, 1804594 (2019).
[2] H. L. Meyerheim *et al.*, Phys. Rev. Lett. **103**, 267202 (2009).

Authors

S. Nakashima, T. Miyamachi, Y. Tatetsu[a], Y. Takahashi, Y. Takagi[b], Y. Gohda[a], T. Yokoyama[b], F. Komori
[a]Tokyo Institute of Technology
[b]Institute for Molecular Science

Nanoscale Potential Mapping: Direct Visualization of Electrical Resistance at Single Surface Steps

Hasegawa Group

Atomically-thin two dimensional electron systems (2DES) have been one of the hot topics because of their unique properties originating from the low dimensionality and reduced symmetry. Among them 2DES by metallic surface states, which are formed by a few monolayer (ML) deposition of metallic elements on semiconducting substrates, have a unique status. Because of the thermal stability through the surface reconstruction, self-organized high-quality periodical structures can be formed in macroscopic dimensions. Basic properties such as atomic structure and electronic states can be well characterized by standard surface science techniques including scanning tunneling microscopy (STM). Recent discovery of superconductivity in surface 2DES attracted further attentions.

Net and local misorientations of the substrate from a nominal plane results in the formation of steps on it. Superstructure due to the surface reconstruction inherently forms boundaries that separate domains whose periodical phases are different from each other. Both of the one-dimensional line defects disrupt the periodicity of the surface atomic arrangement and therefore work as a barrier for the electrons across them. In order to investigate the role of the line defects in electrical transport, we measured the nanometer-scale spatial distribution of local electrochemical potential of an archetypical metallic surface states; the 7×7 structure of Si(111) substrates, using an STM-based technique called scanning tunneling potentiometry (STP) [1]. Using STP, we found potential drops clearly at step edges and phase boundaries of the 2D metallic surface, demonstrating the presence of significant electrical resistance there.

Figure 1 shows STM and electrochemical potential images taken simultaneously on the 7×7 surface under the net current flow from the left to the right. A single-height (0.31 nm) steps are observed running from the upper left to the lower right in the topographic image (Fig. 1(a)). In the corresponding potential image (Fig. 1(b)), potential drops are found at the step edges, as more quantitatively presented in the inset cross-sectional plots, which was taken along the dashed A-B line in Fig. 1(a).

The steps are, however, not the only defects that disrupts the electron transport on the surface. In the potential mapping, which exhibits a ladder-like pattern, one notices several potential drops in narrow terraces separated by the steps. The potential drop due to the rungs of the ladders is more clearly displayed in a cross-sectional profile shown in the inset. The rungs correspond to boundaries that separate domains of the 7×7 reconstructed structures whose phases do not match. The potential images indicate that the phase boundaries also have electrical resistance.

From the obtained potential images and their cross-sectional plots, we can quantitatively analyze the conductivity through an individual step and phase boundary. Since the absolute value of the current density is unknown, we cannot measure the terrace, step, or phase boundary conductivity directly. But, their ratio can be estimated precisely. Since in our measurement we used low-doped substrates, the electrical conductance through the substrate is quite small. The poorly conductive substrate safely eliminates the problem of the bulk contributions in our measurements.

We estimated the conductivity ratio of the step to the

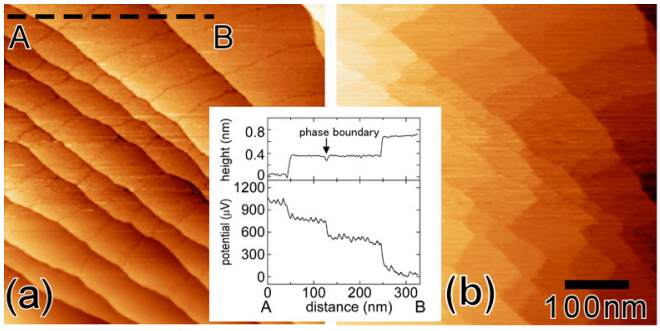

Fig. 1. STM (a) and electrochemical potential (b) images taken simultaneously on the Si(111)7×7 surface. (inset) cross-sectional plots of topographic height and potential taken along the dashed line drawn in (a).

terrace σ_s/σ_t is 3.1±1 /μm. The ratio means that the resistance of a single step corresponds to that the 340 nm-width terrace of the 7×7 structure. This also implies that the contribution of the steps to the net resistance dominates when the tilting angle of the surface exceeds 0.06°, which is much smaller than the tolerance of the miscut angle (~0.16°) for commercial wafers. The macroscopic net resistance through the 7×7 surface states, which include both those of terraces and steps, is therefore basically determined by the step density and the misoriented angle of the substrate.

The phase boundary is found more conductive than the step: the conductivity ratio of a single phase boundary to terrace σ_{ph}/σ_t is 16.4 ± 10 /μm. The density and distribution of phase domains of the 7×7 structure are closely related with nucleation process of the 7×7 structure from disordered 1x1 during the cooling of the sample after the annealing to get rid of the surface oxide layer and to form the clean 7x7 structure. The macroscopic surface conductivity, therefore, also depends on the sample preparation method; e.g. how the sample was slowly cooled after the annealing.

In fact, the electrical conductivity of the surface has been characterized in various methods including microscopic 4-probe methods, but the measured conductivity have been widely dispersed. Our results indicate that the macroscopic net conductivity are mostly determined by the density of steps and domain boundary, thus depending strongly on the misorientation of the sample and its preparation. The present study also demonstrates the importance of characterizing microscopic conductance to elucidate the intrinsic transport properties of the system.

References

[1] M. Hamada and Y. Hasegawa, Jpn. J. Appl. Phys. **51** 125202 (2012).

[2] M. Hamada and Y. Hasegawa, Phys. Rev. B **99**, 125402 1 (2019).

Authors

M. Hamada and Y. Hasegawa

Strain Relaxation at Doped Epitaxial Interfaces

Lippmaa Group

A quasi-two-dimensional quantum well is known to form by electron accumulation at an epitaxial heterointerface between $SrTiO_3$ and $LaAlO_3$. The accumulation of carriers at this interface is the result of a peculiar interplay between several effects, including the polar discontinuity between $SrTiO_3$ and $LaAlO_3$, tetragonal distortion of the interface layer due to the 3% epitaxial strain at the interface, field- and strain-dependent giant dielectric permittivity of $SrTiO_3$, and possibly due to Sr and La intermixing within the first unit cell of the interface. Although the carrier number is essentially fixed by the structure, it is possible to tune the depth distribution of the accumulated carriers by either top- or bottom-side gating, thereby changing the occupancy of the nearly degenerate d_{xy}, d_{xz}, and d_{yz} orbitals. Due to the tetragonal distortion of the interface layer, the orbital degeneracy is partially lifted, lowering the energy of the d_{xy} orbital. Gating can then be used to shift the Fermi level below or above the level crossing, leaving the $d_{xz}/_{yz}$ orbitals either empty or partly filled. One unique feature of this interface is the sharply asymmetric potential profile of the quantum well due to the wide bandgap of $LaAlO_3$. This asymmetry leads to a relatively strong Rashba-type spin-orbit coupling at the interface and this coupling strength can be tuned to some extent by gating, either because the asymmetry of the potential well is changed or due to a Lifshitz transition that occurs when the Fermi level is tuned across the $d_{xy} - d_{xz,yz}$ crossing.

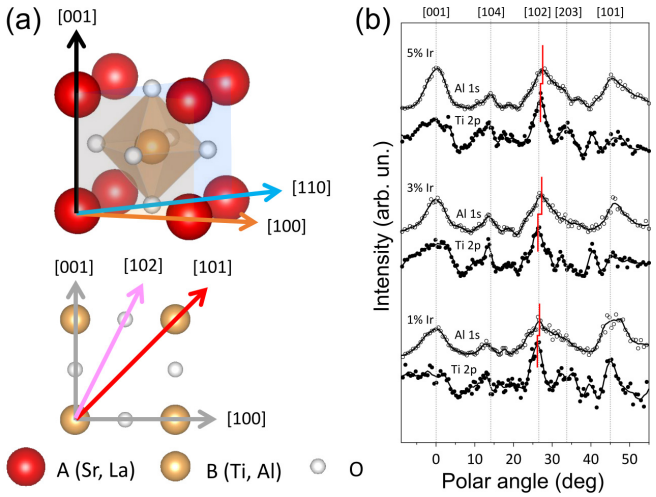

Fig. 1. Crystal FFP orientations. (a) Schematic of sample orientation and the FFP directions in the (010) plane when the emitter is a B-site atom (Al or Ti). (b) XPD polar curves for Ir-doped samples comparing Al 1s and Ti 2p emission signals for different Ir doping levels.

Since this level crossing energy is determined by the tetragonal distortion of the interface layer, we have turned our attention to the possibility of tuning the interfacial strain by doping the interface. Additionally, by adding heavy elements, such as Ir to the interface, it may be possible to control the spin-orbit coupling experienced by the electrons in the quantum well.

$SrTiO_3/LaAlO_3$ heterostructures with interfaces doped either with Ir or Co were grown by pulsed laser deposition and the interfacial strain relaxation was studied by hard (7940 eV) x-ray photoelectron diffraction (XPD) at SPring-8 BL47XU. It was thus possible to estimate the strain state at the interface by comparing XPD forward focusing peak (FFP) positions between La and Sr (perovskite A-site) or Al and Ti (perovskite B-site) (Fig. 1) for different interface doping levels. A shift of the La and Al FFPs towards larger angles relative to Sr and Ti showed that in all cases the $LaAlO_3$ cap layer is under compressive strain in the out-of-plane direction due to epitaxial strain. However, the level of strain depends on interface doping, especially for Ir. One possible cause is the interdiffusion of Ir across the $SrTiO_3/LaAlO_3$ interface. The work suggests that the interfacial strain can be tuned by doping the first unit cell layer of $LaAlO_3$ at the interface with a larger ionic radius cation to reduce the epitaxial strain imposed on the first few unit cells of $SrTiO_3$. This technique may be effective for controlling the critical carrier density where the Lifshitz transition occurs and thus selecting the gate bias range where the spin-orbit coupling in the quantum well is tunable by gating.

Reference

[1] M. Lee, X. L. Tan, M. Yoneda, T. Okamoto, I. Tanaka, Y. Higa, D. Peng, M. Ogi, S. Kobayashi, M. Taguchi, M. Lippmaa, M.-J. Casanove, and H. Daimon, J. Phys. Soc. Jpn. **87**, 084601 (2018).

Authors

M. Lee[a], X. L. Tan[a], M. Yoneda[a], T. Okamoto[a], I. Tanaka[a], Y. Higa[a], D. Peng[a], M. Ogi[a], S. Kobayashi[a], M. Taguchi[a], M. Lippmaa, M.-J. Casanove[b], and H. Daimon[a], J. Phys. Soc. Jpn. 87 (2018) 084601

[a]Nara Institute of Science and Technology

[b]University of Toulouse

CO_2 Activation and Reaction on Zn-Deposited Cu Surfaces Studied by Ambient-Pressure X-Ray Photoelectron Spectroscopy

Yoshinobu and I. Matsuda Groups

It is important to understand the mechanisms of activation and hydrogenation of carbon dioxide (CO_2) in order to utilize the abundant CO_2 effectively as a chemical feedstock. One way of utilizing CO_2 is methanol synthesis on Cu-based catalysts. Metallic copper in the catalysts is considered to be an active site for methanol synthesis. So far, the adsorption and reaction of CO_2 on Cu surfaces have been widely investigated under ultrahigh vacuum (UHV) and under ambient pressure conditions.

In this study [1], the reaction of CO_2 on Zn-Cu(111) and Zn-Cu(997) was systematically studied using ambient-pressure X-ray photoelectron spectroscopy (AP-XPS) at SPring-8 BL07LSU (2015B7496 and 2016A7401). AP-XPS allows adsorbate and substrate electronic states to be elucidated under reaction conditions. The aim of this study is to reveal the roles of Zn and water in the CO_2 reaction, and elementary steps of methanol synthesis by a series of systematic experiments performed under well-defined conditions at temperature between 299-473 K. We used Zn-deposited Cu(111) and Cu(997) single crystals as model catalytic systems. Stepped Cu surfaces are more reactive for dissociation of CO_2 compared to flat Cu surfaces. Recently, we have investigated adsorption states of CO_2 on Cu(997) surfaces under UHV, and near-ambient condition. In this study, we have focused on hydrogenation of CO_2 under near-ambient pressure conditions to clarify the effect of the step sites. The oxidation state of Zn-deposited Cu surfaces and the stability of reaction products depend strongly on the gas composition and sample temperature. The effect of water on the CO_2 activation was also examined by a set of control experiments.

In the presence of 0.8 mbar CO_2 and 0.4 mbar H_2 gases, hydrogenation products are not observed; only carbonate is formed on Zn-deposited Cu(111) and Cu(997) surfaces (not shown here). We found that the formation rate of carbonate at 299 K is significantly faster on Zn/Cu(997) than that on Zn/Cu(111), indicating that *step sites are more reactive for CO_2 activation than terrace sites*. On the other hand, the addition of water (D_2O) in the feed gas leads to hydrogenation of CO_2 to formate at sample temperatures around 400 K (Fig. 1). This suggests that hydroxyl produced from dissociative adsorption of water is a reactant in the CO_2 hydrogenation observed under the present reaction conditions. Figure 2 schematically shows the proposed reactions on the Zn-deposited Cu surface in the presence of CO_2, H_2 and H_2O. We also found that the reaction products such as carbonate and formate on the Zn/Cu(997) surface are more stable than those on the bare Cu(997) surface. In particular, formate remains on Zn-deposited Cu surfaces up to 473 K, which is close to the operation temperature of industrial Cu-ZnO catalysts. We conclude that *an important role of Zn on Cu surfaces is the stabilization of reaction intermediates originated from CO_2*.

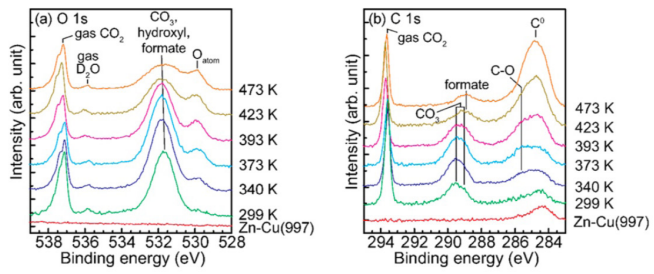

Fig. 1. A series of XPS spectra on Zn(0.25 ML)/Cu(997) surface: (a) O 1s and (b) C 1s. The spectra of bare Zn-Cu(997) surface were measured under UHV. AP-XPS measurements were first performed at 299 K in the presence of 0.8 mbar CO_2, 0.4 mbar H_2, and 0.05 mbar D_2O, then the sample was heated up to 473 K under this ambient-pressure condition.

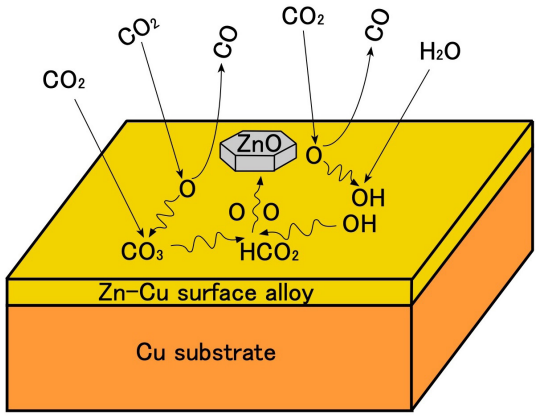

Fig. 2. Schematic diagram of proposed reactions on the Zn-deposited Cu surface in the presence of CO_2, H_2 and H_2O.

Reference
[1] T. Koitaya, S. Yamamoto, Y. Shiozawa, Y. Yoshikura, M. Hasegawa, J. Tang, K. Takeuchi, K. Mukai, S. Yoshimoto, I. Matsuda, and J. Yoshinobu, ACS Catal. **9**, 4539 (2019).

Authors
T. Koitaya[a], S. Yamamoto, I. Matsuda, and J. Yoshinobu
[a]Institute for Molecular Science (present address)

Biophysical Study on the Function and Molecular Mechanism of Rhodopsins

Inoue Group

Rhodopsin is photo-receptive heptahelical transmembrane proteins in which retinal chromophore is covalently bound to a conserved lysine residue in the seventh helix, and animal and microbial rhodopsin families are known so far. Animal rhodopsins present in animal retina transfer visual signal to brain and are also related to non-visual light sensing. Microbial rhodopsins show diverse functions: light-driven ion pump, light-gated ion channels, light-regulated enzyme and so on. Both types of rhodopsins are being widely used in optogenetics to control various cellular events, such as neural activity, gene expression and so on, by light. Recently, we reported third class of rhodopsin, heliorhodopsin (HeR), which is evolutionally isolated from both of microbial and animal rhodopsins [1]. The biochemical study revealed its inverted structure compared with other class of rhodopsins, and N- and C-termini of HeR faces extracellular and cytoplasmic milieus, respectively (Fig. 1). HeRs are diversely distributed from bacteria, archaea, eukaryotic algae and giant viruses. Although the function of HeR has not been clarified yet, we observed a long photo-reaction cycle up to seconds to minutes by laser flash photolysis suggesting HeR works as a signaling protein which transfers light signal to unidentified intracel-

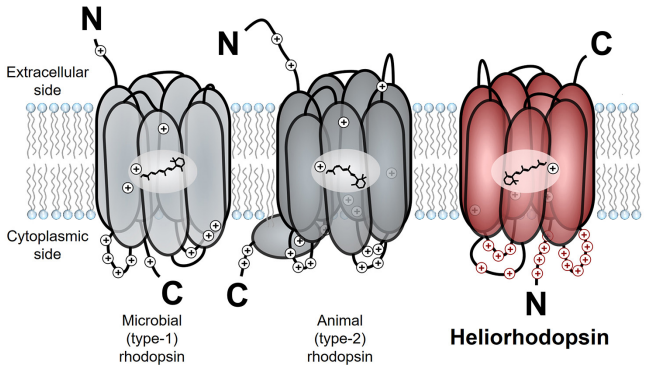

Fig. 1. Molecular structures of microbial rhodopsin, animal rhodopsin and heliorhodopsin.

lular proteins. The retinal chromophore in HeR isomerizes from all-*trans* to 13-*cis* form upon light illumination, and we dominantly observed K, M and O-intermediates in the photocycle. While the K and O intermediates show red-shifted absorption compared with that of the dark state, the absorption of M-intermediate is highly blue-shifted to 400 nm and a proton is released from retinylidene Schiff-base. A mutational study suggested that the proton is not transferred to a specific residue and it is trapped in a hydrogen bonding network, called proton accepting group (PAG), constituted from several amino-acid residues including conserved histidines and internal water molecules on the extracellular side of the protein.

Rhodopsins show wide range of absorption wavelength and the color regulation of retinal chromophore in rhodopsins to achieve longer-wavelength absorption is one of critical elemental technique to develop new types of optogenetics tools which can avoid strong light-scattering by biological tissues and phototoxicity. We reported that the mutation of the conserved proline and serine residues in sodium pump rhodopsin (KR2) induces 40-nm red-shift of the absorption without impairing sodium-transport activity [2]. Also, FTIR spectroscopy and quantum mechanical calculation revealed that the change in dipole moments of these residues lowered energy gap of π-electron of retinal chromophore by electrostatic interaction. Furthermore, we identified a new type of sodium pump rhodopsin from α-proteobacterium, *Jannaschia seosinensis*, in which the proline residue was naturally altered to glycine and it shows 20-nm longer absorption than that of KR2. Since *J. seosinensis* is derived from solar saltern, the natural mutation of the proline occurred to use longer wavelength light in turbid environment. Since sodium pump rhodopsin can suppress the neural spiking without alterations of intracellular pH and Cl^- concentration, this red-shifted KR2 would be expected to be applied as a new type of optogenetic tool.

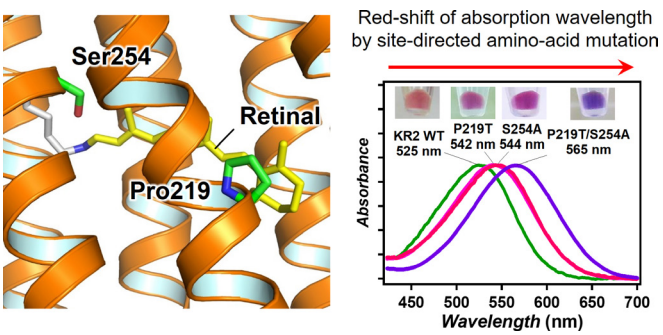

Fig. 2. Construction of light-driven sodium pump rhodopsin absorbing longer-wavelength light by site-directed amino-acid mutagenesis

References
[1] A. Pushkarev, K. Inoue *et al*., Nature **558**, 595 (2018).
[2] K. Inoue, M. d. C. Marín *et al*., Nat. Commun. **10**, 1993 (2019).

Author
K. Inoue

Emergent SU(4) Symmetry and Quantum Spin-Orbital Liquid in α-$ZrCl_3$

Oshikawa Group

As materials are cooled down towards the absolute zero temperature, generally they become a solid with a long-range order in location of atoms. Likewise, magnetic materials develop a magnetic long-range order at sufficiently low temperatures. However, we may expect a "quantum spin liquid" as a ground state of a magnetic material, if strong quantum fluctuations destroy the magnetic order even at zero temperature. Theoretical studies have revealed that quantum spin liquids exhibit various exotic phenomena such as fractionalization. Its realization has been one of the central topics in quantum magnetism and condensed matter physics. After intensive studies over several decades, several materials have been found to be strong candidates of quantum spin liquids. However, such candidate materials are still limited, and it is desirable to find new class of quantum spin liquid materials.

Quantum magnets often possess the (approximate) spin rotation symmetry. Mathematically it corresponds to the group of "rotations" of two-component complex vectors, SU(2). Here the two components of the vector correspond to the amplitudes of the spin pointing up and down. It is then natural to consider an extended symmetry of "rotations" of N-component complex vectors, SU(N). For a larger N, the symmetry is larger, and the quantum fluctuations would be stronger. In fact, there have been numerous theoretical studies of SU(N) "spin" systems, many of which are found to be quantum spin liquids. Experimentally, the SU(N) symmetry has been realized using nuclear spin degrees of freedom in cold atoms. However, it is still difficult to observe the SU(N) quantum spin liquid behavior in cold atoms, it is desirable to realize it in a magnetic material.

In principle, the SU(N) symmetry can appear if there are degenerate orbitals which can be occupied by electrons. For example, there are two degenerate orbitals in each atom, an electron can take 2 orbital states and 2 spin states, namely 4 states in each atom. If the system is symmetric with respect to the "rotation" of these 4 states, it is SU(4) symmetric.

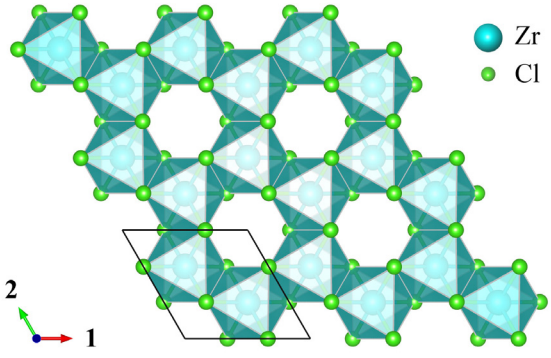

Fig. 1. Crystal structure of α-$ZrCl_3$. Zr^{3+} ions form a honeycomb lattice.

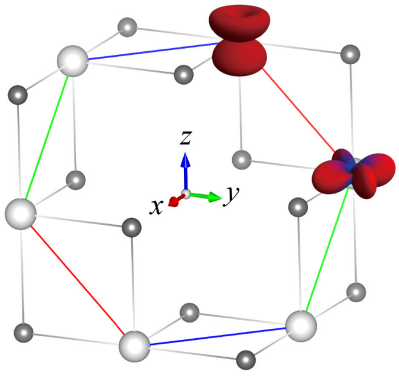

Fig. 2. Hexagonal plaquette of α-$ZrCl_3$. Hoppings between anisotropic d-orbitals are strongly orbital-dependent, and also depend on the bond directions indicated by colors (red, blue, and green).

However, since the orbital and spin are completely different degrees of freedom, there is no particular reason to expect the SU(4) symmetry. In fact, it has been known that the standard model of electrons in the presence of two degenerate orbitals, Kugel-Khomskii model, has the SU(4) symmetry only at a special point, which would require a fine-tuning. Indeed, no material has been known to possess the SU(4) symmetry, even approximately.

In this work [1], we demonstrate theoretically that the SU(4) symmetry emerges in α-$ZrCl_3$ (Fig.1). In the limit of strong spin-orbit coupling, the effective model of electrons in this material has strongly orbital-dependent hoppings (Fig. 2). As a result, the model looks far from SU(4) symmetric. However, the electron hopping between neighboring Zr ions can be identified with an SU(4) gauge field on the lattice. We find that, with an appropriate SU(4) gauge transformation on the lattice, the model is mapped to a manifestly SU(4)-symmetric one (Kugel-Khomskii model at the SU(4) point). This means that α-$ZrCl_3$ has an emergent SU(4) symmetry, despite the strong spin-orbit coupling which seems to destroy even the spin SU(2) symmetry. In the strong electron repulsion limit, the effective model is reduced to the SU(4) "antiferromagnetic Heisenberg" model, which has a gapless spin liquid ground state according to a preceding theoretical study. Therefore, we expect that α-$ZrCl_3$ realizes an SU(4)-symmetric quantum spin liquid. In fact, the SU(4) symmetry means that the spin and orbital degrees of freedom are intertwined and fluctuating together. In this sense, the ground state should be better called a quantum spin-orbital liquid.

Reference

[1] M. Yamada, M. Oshikawa, and G. Jackeli, Phys. Rev. Lett. **121**, 097201 (2018).

Authors
M. Yamada, M. Oshikawa, and G. Jackeli[a]
[a]University of Stuttgart and Max-Planck Institute for Solid State Research

Tuning of Luttinger Semimetal into Weyl Semimetal by Strain and Magnetic Field

Nakatsuji, Lippmaa, Katsumoto, and Kindo Groups

In the field of condensed matter physics, there has been an intense search for topological nontrivial electronic phases in strongly correlated materials. To date, most research on topological electronic systems has been limited to weakly correlated materials where electronic correlations play a minor role. Among newly-found topological phases, the Weyl semimetal phase has attracted the most significant attention because the Weyl fermions exhibit extremely high electrical and thermal conductivities, which may find use in ultrahigh-speed and low-power consumption devices. While the Weyl semimetal phase was experimentally discovered in the inversion symmetry broken TaAs system in 2015 [1,2], only a few candidates of the magnetic version have been found in systems with broken time reversal symmetry. Historically, a magnetic Weyl system is the first Weyl semimetal predicted for condensed matter in 2012 in the seminal paper by Wan *et al*. [3]. Notably, this prediction was specifically made for the pyrochlore iridates.

Here, we focus on a pyrochlore iridate $Pr_2Ir_2O_7$. This material is known as a Luttinger semimetal where electronic correlations are strong [4]. According to theoretical predictions, the electronic state can be tuned into a Weyl semimetal state by perturbations such as lattice strain and external magnetic field [5,6]. However, experimental proof of the existence of the Weyl semimetal remains elusive because it is difficult to apply uniaxial strain on bulk single crystals. One possible solution to this problem is to use $Pr_2Ir_2O_7$ thin films where lattice strain can be introduced through epitaxy. To that end, more than 10 groups around the world have been working on fabricating $Pr_2Ir_2O_7$ thin films, but there have been no reports of success.

What makes the fabrication of the thin films difficult is the high volatility of iridium, especially at high temperatures. We therefore turned to solid-state epitaxy, namely, the deposition of precursors at room temperature by pulsed laser deposition followed by annealing in air. This synthesis route mimics bulk crystal growth and allowed us to successfully fabricate high-quality epitaxial thin films of pyrochlore $Pr_2Ir_2O_7$ on yttria-stabilized zirconia substrates [7]. Detailed crystal structure analysis revealed that strained and relaxed grains coexisted in the films. When Hall measurements were performed using the $Pr_2Ir_2O_7$ films, spontaneous Hall effect was found below 50 K even though the material shows no spontaneous magnetization nor was an external magnetic field applied to the film. This temperature of 50 K is very high, considering that bulk single crystals show spontaneous Hall effect only below 1.5 K [8]. The spontaneous Hall effect appears due to the all-in-all-out structure of the iridium 5*d* moments and the associated time reversal symmetry breaking. In this case, the theoretically predicted condition that the Weyl semimetal state appears when both the cubic symmetry and the time reversal

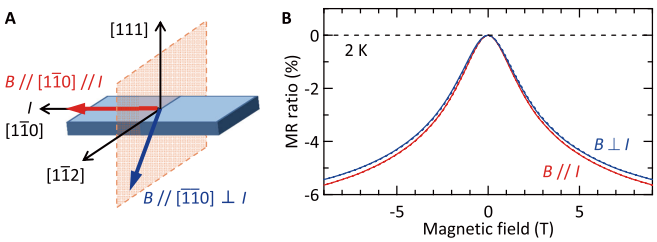

Fig. 1. Additional contribution to the negative longitudinal magnetoresistance for a $Pr_2Ir_2O_7$ thin film. (A) Experimental configurations. *B* and *I* represent the external magnetic field and current, respectively. For the longitudinal (*B* // *I*) and transverse (*B* ⊥ *I*) cases, *B* is applied along the [1$\bar{1}$0] and [$\bar{1}$10] direction, respectively. *I* flows along the [1$\bar{1}$0] direction in both cases. (B) Magnetoresistance curves as a function of *B* measured at 2 K for *B* // *I* and *B* ⊥ *I* configurations. The solid and dotted lines correspond to up and down sweeps of *B*, respectively. The difference between the two curves comes from the chiral anomaly and indicates that the film is in the Weyl semimetal state.

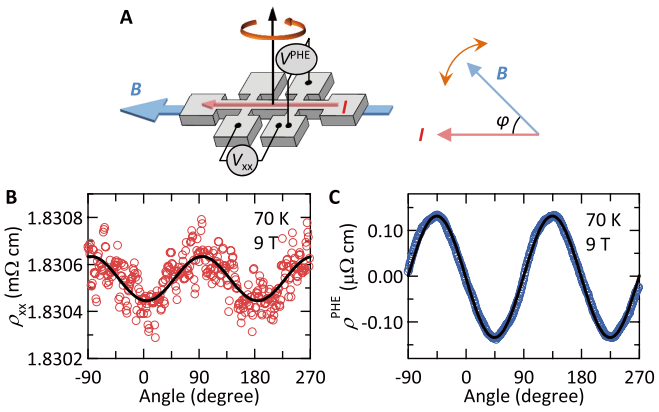

Fig. 2. Planar Hall effect in a $Pr_2Ir_2O_7$ thin film. (A) Experimental configuration. *I* flows along the [1$\bar{1}$0] direction and *B* is applied in the same plane. The angle between *I* and *B* (φ) is changed by the in-plane rotation of the sample. The longitudinal and planar Hall resistance is measured by V_{xx} and V^{PHE}, respectively. (B and C) Angle dependence of the longitudinal and planar Hall resistivity, respectively, measured at 70 K and 9 T. The red and blue open circles are the experimental data, and the black solid lines are the fitting results using the equations predicted theoretically [10,11]. The experimental results agree well with the theory, suggesting that the film has been tuned into the Weyl semimetal state.

symmetry are broken is satisfied in the strained grains in the film. On the other hand, although the relaxed grains are in the Luttinger semimetal state, it is possible that they can be tuned into a magnetic Weyl semimetal when an external magnetic field is applied and the time reversal symmetry is broken. To confirm this, we examine the effects of the chiral anomaly, which is the magneto-electric response of the Weyl semimetal. As a result, we find strong evidence for the chiral anomaly in the negative longitudinal magnetoresistance [9] (Fig. 1) and the planar Hall effect [10,11] (Fig. 2). This means that the Luttinger semimetal can be modified into the Weyl semimetal by an external magnetic field.

In summary, we have successfully fabricated epitaxial thin films of $Pr_2Ir_2O_7$ and experimentally demonstrated that the Weyl semimetal state can be induced either by lattice strain or by applying an external magnetic field. Based on the results with the Luttinger semimetal, the research for the topological phases in strongly correlated systems, which has not been done so far, will proceed. It is expected to lead to the development of ultrahigh-speed and low-power devices utilizing the Weyl fermions having high electric and thermal conductivities.

References
[1] B. Q. Lv *et al.*, Phys. Rev. X **5**, 031013 (2015).
[2] S.-Y. Xu *et al.*, Science **349**, 613 (2015).
[3] X. Wan *et al.*, Phys. Rev. B **83**, 205101 (2011).
[4] B. Cheng, T. Ohtsuki *et al.*, Nat. Commun. **8**, 2097 (2017).
[5] E.-G. Moon *et al.*, Phys. Rev. Lett. **111**, 206401 (2013).
[6] T. Kondo *et al.*, Nat. Commun. **6**, 10042 (2015).
[7] T. Ohtsuki *et al.*, Proc. Natl. Acad. Sci. U.S.A. **116**, 8803 (2019).
[8] Y. Machida *et al.*, Nature **463**, 210 (2010).
[9] D. T. Son and B. Z. Spivak, Phys. Rev. B **88**, 104412 (2013).
[10] A. A. Burkov, Phys. Rev. B **96**, 041110(R) (2017).
[11] S. Nandy *et al.*, Phys. Rev. Lett. **119**, 176804 (2017).

Authors
T. Ohtsuki, Z. Tian, A. Endo, M. Halim, S. Katsumoto, Y. Kohama, K. Kindo, M. Lippmaa, and S. Nakatsuji

Strong Electronic Correlations in a Luttinger Semimetal $Pr_2Ir_2O_7$

Nakatsuji Group

In the field of the solid state physics, materials exhibiting novel physical properties are vigorously explored. Zero-gap semiconductors are one fascinating group of materials where topological functionalities lead to high carrier mobility and the quantum Hall effect. It is known that electrons behave as if they are massless in materials such as graphene because of the linear band dispersion near the point where the valence and the conduction bands come in contact with each other. For graphene, new phenomena were discovered one after another and it became the subject of the Nobel Prize in Physics in 2010. So far, the physics of zero-gap semiconductors have only been studied in materials where the interaction between electrons is weak.

An example of a zero-gap structure is a Luttinger semimetal with quadratic band touching whose band dispersion is parabolic near the band touching point as illustrated in Fig. 1. It was predicted more than 40 years ago that materials in a Luttinger semimetal state would show novel electronic states because of the strong electronic correlations that are unobtainable in conventional metals. However, in materials known so far, such as α–Sn and HgTe, it has been difficult to identify experimentally the effects of electronic correlations because the effective mass of electrons is small and hence the electronic correlations are weak.

To clarify the effect of the strong electronic correlations, we focused on $Pr_2Ir_2O_7$ [1]. It is already known that $Pr_2Ir_2O_7$ is a Luttinger semimetal with quadratic band touching and that the effective mass of electrons is about 6 times larger than the mass of the free electron in vacuum [2]. We therefore carried out a terahertz spectroscopy study on the $Pr_2Ir_2O_7$ thin films and observed a very large dielectric constant of about 180 at a temperature of 5 K as shown in Fig. 2 [3]. This value is several tens of times larger than that of zero-gap semiconductors (e.g. α–Sn and HgTe) known so far. Additionally, in a Luttinger semimetal state, the dielectric constant is a measure of the scale of electronic correlations. By using this fact, when the magnitude of the electronic correlations is estimated from the dielectric constant, the scale of electronic correlations is about 2 orders of magni-

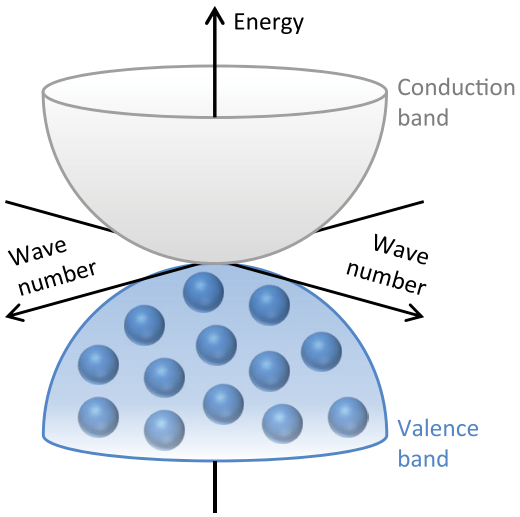

Fig. 1. Band structure of a Luttinger semimetal, which is a zero-gap semiconductor. The valence band, which is filled with electrons (blue spheres) and the empty conduction band both have a three-dimensional parabolic shape, and are in contact with each other at a single point close to the Fermi level.

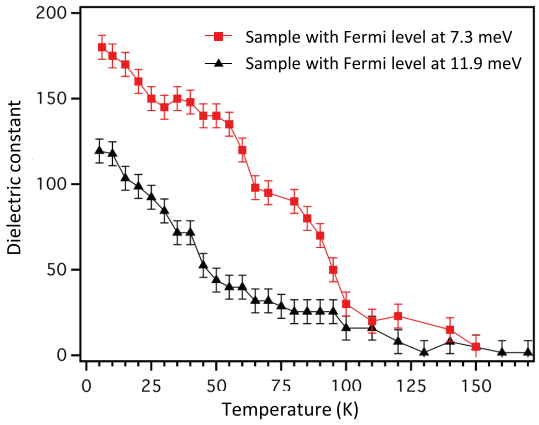

Fig. 2. Temperature dependence of the dielectric constant. The low-temperature value is several tens of times larger than that of known zero-gap semiconductors (e.g. α–Sn and HgTe). The dielectric constant becomes larger when the Fermi level approaches the band touching point.

tude larger than the kinetic energy.

We have thus demonstrated that electronic correlations are indeed very strong in a Luttinger semimetal with quadratic band touching. In the future, it is expected that further understanding of the role of electronic correlations in determining the physical properties of zero-gap semiconductors will lead to the creation of novel metallic states and new functional materials.

References
[1] T. Ohtsuki *et al.*, Proc. Natl. Acad. Sci. U.S.A. **116**, 8803 (2019).
[2] T. Kondo *et al.*, Nat. Commun. **6**, 10042 (2015).
[3] B. Cheng, T. Ohtsuki *et al.*, Nat. Commun. **8**, 2097 (2017).

Authors
T. Ohtsuki, B. Cheng[a], D. Chaudhuri[a], S. Nakatsuji, M. Lippmaa, and N. P. Armitage[a]
[a]The Johns Hopkins University

Large Spin Hall Effect in Amorphous Mn-Sn Alloy Thin Film

Nakatsuji Group

Pure spin current contains only angular momentum without net charge flow, which greatly reduces the Joule heating. This feature makes spin current beneficial for low power spintronic devices. The spin Hall effect (SHE) converts charge current to transverse spin current, serving as an effective way to generate pure spin current. Meanwhile, as the reciprocal effect of the SHE, the inverse spin Hall effect (ISHE) converts pure spin current to transverse charge

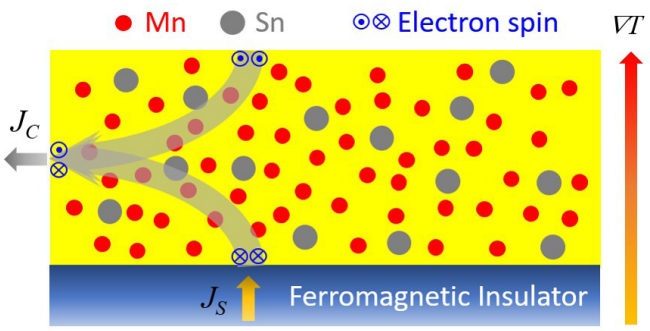

Fig. 1. Schematic of thermal spin injection from a ferromagnetic insulator into an attached metal layer.

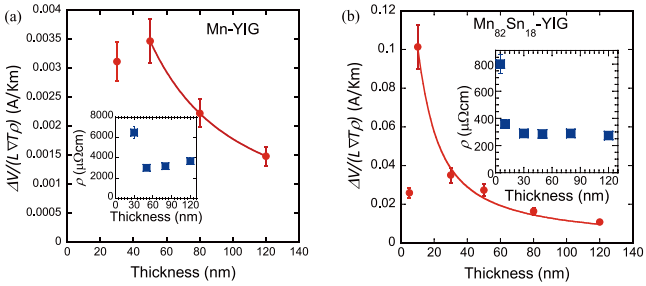

Fig. 2. Thickness dependent thermal voltage for (a) Mn and (b) Mn-Sn alloy thin films on YIG. Insets are thickness dependence of resistivity.

current, and plays an important role in pure spin current detection and conversion.

Although manipulation of pure spin current in heavy transition metals, ferromagnetic metals, and their alloys have been extensively explored in the past decade, antiferromagnets have become a new central stage due to its prominent advantages such as high frequency magnetic dynamics, negligible stray field, and perturbation insensitivity. Among these materials, the non-collinear Kagome lattice antiferromagnets Mn_3X (X = Sn, Ge, Ga) stand out because of their large transverse electrical [1-4] and optical [5] responses to the external magnetic field as well as their negligible magnetic moment.

In our work, we used the thermally generated pure spin current from the spin Seebeck effect (SSE) in the ferrimagnetic insulator yttrium iron garnet (YIG) to study the inverse spin Hall effect in Mn and the Mn-Sn alloys (Fig. 1). A series of samples with different thicknesses are sputtering deposited onto YIG substrates. By measuring the ISHE voltage, we obtained a sizable spin Hall angle θ_{SH} of -0.23% (which measures the conversion efficiency between charge current and spin current), and a long spin diffusion length $\lambda_{sd} \approx 11.5$ nm for the single element material Mn, as shown in Fig. 2 (a). Most importantly, by doping Sn in Mn, we found that the θ_{SH} of the Mn-Sn alloy, even in its *amorphous* form, is increased by 20 times to -4.4%, while the resistivity (ρ) is reduced by about 10 times, as shown in Fig. 2 (b). Therefore, the energy consumption ($\sim\rho/\theta^2_{SH}$) of the Mn-Sn alloy is reduced by 4000 times compared to Mn. A spin pumping measurement further corroborates the enhancement of the θ_{SH} in the Mn-Sn alloy. These results not only serve as essential references in studying the pure spin current phenomena in Mn-based alloys, but also offer a promising method for exploring future energy efficient spin Hall materials with high spin Hall angle but low resistivity and thus low energy consumptions [6].

References
[1] S. Nakatsuji, N. Kiyohara, and T. Higo, Nature **527**, 212 (2015).
[2] M. Ikhlas, T. Tomita *et al.*, Nat. Phys. **13**, 1085 (2017).
[3] N. Kiyohara, T. Tomita, and S. Nakatsuji, Phys. Rev. Appl. **5**, 064009 (2016); A. K. Nayak *et al.*, Sci. Adv. **2**, e1501870 (2016).
[4] Z. H. Liu *et al.*, Sci. Rep. **7**, 515 (2017).
[5] T. Higo *et al.*, Nat. Photon. **12**, 73 (2018).
[6] D. Qu, T. Higo, T. Nishikawa, K. Matsumoto, K. Kondou, P. K. Muduli, Y. Otani, and S. Nakatsuji, Phys. Rev. Mater. **2**, 102001(R) (2018).

Authors
D. Qu, T. Higo, T. Nishikawa, K. Matsumoto, K. Kondou[a], D. Nishio-Hamane, R. Ishii, P. K. Muduli, Y. Otani and S. Nakatsuji
[a]RIKEN-CEMS

Large Anomalous Hall Effect in Thin Films of a Weyl Magnet Mn_3Sn

Nakatsuji and Otani Groups

Recently, there has been a surge of interest in antiferromagnets (AFMs) as prospective spintronic materials for high-density and ultrafast memory devices because of their vanishingly small stray field and orders of magnitude faster spin dynamics compared to their ferromagnetic counterparts. In particular, the recently discovered functional antiferromagnet $D0_{19}$ Mn_3Sn has attracted broad attention as the first example of a magnetic Weyl material/Weyl magnet [1-5]. This material exhibits a variety of useful functions that have never been observed before in antiferromagnets at zero magnetic field, including the anomalous Hall effect [1], the anomalous Nernst effect [2], and the magneto-optical Kerr effect [5] at room temperature. All these properties are controllable by a magnetic field and thus can be used for designing antiferromagnetic spintronics and in energy harvesting technology. It has been shown that such an antiferromagnet hosts a topological state characterized by magnetic Weyl fermions [3,4]. The discovery of the Weyl metal state in an antiferromagnet opens up a new chapter of applied research using the functional antiferromagnets. Therefore, fabrication of high quality thin films of the Weyl antiferromagnet becomes all the more important.

For the thin film fabrication, we employ DC magnetron sputtering. The films (40-400 nm) are deposited at room temperature onto a Si/SiO_2 substrate from the Mn_3Sn target. After the deposition at room temperature, we anneal the film at 500ºC for one hour, and thereby crystallizes the as-deposited amorphous film in a polycrystalline form of the Mn_3Sn film. XRD measurements reveal that the films are the single phase of Mn_3Sn and are in a randomly oriented polycrystalline form; all the peaks can be indexed by the hexagonal $P6_3/mmc$ symmetry of $D0_{19}$ Mn_3Sn, with no additional peaks due to plausible impurity phases (Fig.1(a)).

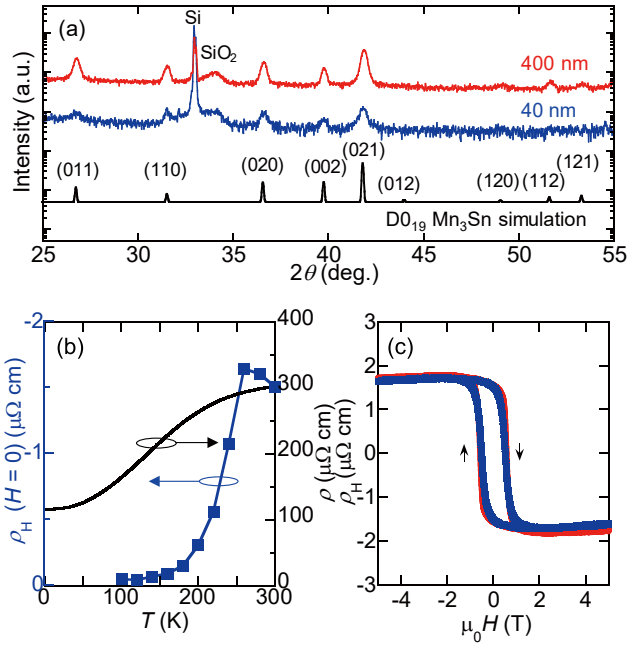

Fig. 1. (a) Room temperature spectra obtained with an X-ray diffractometer for the 40 and 400 nm thin films of Mn_3Sn on a Si/SiO_2 substrate. The theoretical spectrum of the $D0_{19}$ Mn_3Sn structure is shown at the bottom. (b) Temperature dependence of the resistivity ρ and the spontaneous Hall resistivity ρ_H of the Mn_3Sn (40 nm) thin film. (c) Field dependence of the Hall resistivity ρ_H measured under a magnetic field applied in the perpendicular direction to the surface of the Mn_3Sn thin films.

Figure 1(b) shows the temperature dependence of the longitudinal resistivity ρ and the spontaneous Hall resistivity ρ_H (H = 0) of the Mn_3Sn thin film under zero field. The behavior of longitudinal resistivity ρ confirms the metallic transport consistent with the previous work on bulk single crystals [2]. The zero-field Hall resistivity ρ_H (H = 0) was obtained from (ρ_H (H = +0) - ρ_H (H = -0))/2. (Here, we use +0 and -0 to indicate zero magnetic field approached, respectively, from +5 T and -5 T in the Hall resistivity measurement at each temperature.) We have observed a sharp decrease in ρ_H (H = 0) below T_1 = 260 K on cooling; this behavior agrees with the magnetic symmetry consideration in Mn_3Sn that the inverse triangular spin structure breaks the global time-reversal symmetry, whereas time-reversal symmetry is restored in the low temperature helical phase. Figure 1(c) displays the field dependence of the Hall resistivity ρ_H (H) at 300 K as a function of the magnetic field applied perpendicular to the film surface. The anomalous Hall effect of the Mn_3Sn films exhibit a significant change in ρ_H (H) from 1.5 μΩcm to -1.5 μΩcm with increasing field despite the vanishingly small magnetization; this feature is generated by the switching of the antiferromagnetic domain in real space and the large fictitious field in momentum space [6]. Notably, this is the first report on the thin film of the antiferromagnetic Mn_3Sn film exhibiting the large anomalous Hall effect of the same order of magnitude as the value reported for bulk. Our fabrication of the high-quality thin film of the Weyl magnet Mn_3Sn and the observation of its large anomalous Hall effect provide an important step to further develop devices useful for antiferromagnetic spintronics, such as for high-speed and high-density information storage.

References

[1] S. Nakatsuji, N. Kiyohara, and T. Higo, Nature **527**, 212 (2015).
[2] M. Ikhlas, T. Tomita *et al*., Nat. Phys. **13**, 1085 (2017).
[3] K. Kuroda, T. Tomita *et al*., Nat. Mater. **16**, 1090 (2017).
[4] H. Yang *et al*., New J. Phys. **19**, 015008 (2017).
[5] T. Higo *et al*., Nat. Photon. **12**, 73 (2018).
[6] T. Higo, D. Qu, Y. Li, C. L. Chien, Y. Otani, and S. Nakatsuji, Appl. Phys. Lett. **113**, 202402 (2018).

Authors

T. Higo, D. Qu, Y. Li[a], C. L. Chien[a], Y. Otani, and S. Nakatsuji

[a]Johns Hopkins University

Giant Anomalous Nernst Effect at Room Temperature in a Weyl Ferromagnet

Nakatsuji Group

The anomalous Nernst effect (ANE) is a well-known thermoelectric effect for ferromagnets, namely the generation of an electric voltage perpendicular to both magnetization and an applied temperature gradient. This transverse geometry of ANE leads to various advantages for thermoelectric modules compared to the conventional one based on Seebeck effect, such as simpler structure to efficiently cover a heat source, higher flexibility, lower production cost, and larger conversion efficiency for the same figure of merit [1]. However, the size of ANE is generally very small (on the order of ~0.1 μV/K), which hinders its practical applications. Recent theoretical and experimental investigations on topological materials indicate that the intense Berry curvature of Weyl points near the Fermi energy can enhance the intrinsic ANE, rendering ANE an powerful probe to

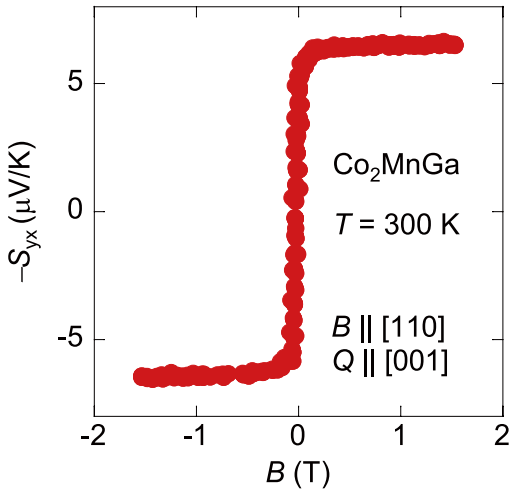

Fig. 1. Magnetic field dependence of anomalous Nernst coefficient of Co_2MnGa at room temperature.

clarify the topological electronic structure in magnetic Weyl semimetals [2-4]. In other words, a ferromagnet exhibiting a giant ANE may serve as an ideal ground for magnetic Weyl semimetal state.

In this work, we report the giant ANE in a full-Heusler ferromagnet Co_2MnGa, reaching a record high value of S_{yx} ~6 μV/K at room temperature [5] (Fig. 1). The crossover from Mott relation $\alpha_{yx} \sim T$ to $-\ln T$ dependence is observed on warming, where α_{yx} is the transverse thermoelectric conductivity, indicating the proximity to the quantum Lifshitz transition between type-I and type-II magnetic Weyl fermion states. Out study provides a new guideline for searching new topological magnets which are useful for energy harvesting and spintronics.

References

[1] M. Mizuguchi and S. Nakatsuji, Sci. Tech. Adv. Mater. **20**, 262 (2019).
[2] D. Xiao *et al*., Rev. Mod. Phys. **82**, 1959 (2010).
[3] M. Ikhlas *et al*., Nat. Physics **13**, 1085 (2017).
[4] K. Kuroda *et al*., Nat. Mater. **16**, 1090 (2017).
[5] A. Sakai *et al*., Nat. Physics **14**, 1110 (2018).

Authors

A. Sakai, Y. P. Mizuta[b,c], A. A. Nugroho[d], R. Sihombing[d], T. Koretsune[a,c], M.-T. Suzuki[a,c], N. Takemori[c], R. Ishii, D. N.-Hamane, R. Arita[a,c], P. Goswami[e,f], and S. Nakatsuji[a]

[a]CREST, Japan Science and Technology Agency (JST)
[b]Kanazawa University
[c]Center for Emergent Matter Science, RIKEN
[d]Bandung Institute of Technology
[e]University of Maryland
[f]Northwestern University

Magnetic Spin Hall Effect in a Non-Collinear Antiferromagnet

Otani and Nakatsuji Groups

The conventional spin Halle effect (SHE) converts electrical currents to transverse spin currents in non-magnetic conductors in response to an electric field. The SHE has thus drawn much attention as a means to switch the magnetization of the adjacent ferromagnetic layer via spin orbit torque. New functions have been further explored in various materials in terms of spin-charge currents interconversion. The magnetic contribution to the SHE has therefore

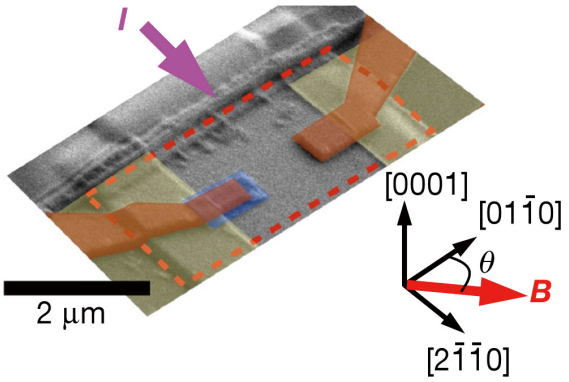

Fig. 1. Scanning electron microscope image of the spin-accumulation device. The microfabricated Mn_3Sn single crystal is indicated by the red dashed line. A NiFe ferromagnetic electrode and non-magnetic Cu electrodes are indicated by blue and brown areas, respectively. The edge of the Mn_3Sn crystal indicated by yellow area is covered with a 30-nm-thick Al_2O_3 insulating layer to avoid electrical contact at the edge.

been studied intensively in these days. Here we show that antiferromagnets have richer spin Hall properties than that of non-magnetic materials. The material focused on here is Mn_3Sn, which shows non-collinear antiferromagnetic order of Mn magnetic moments that have an inverse triangular spin configuration on stacked kagome lattices [1]. We find non-trivial time reversal-symmetry-breaking counterparts of the conventional SHE, which is called magnetic spin Hall effect [2].

To study the SHE in a non-collinear antiferromagnet, we fabricated a device consisting of ferromagnetic NiFe and non-magnetic Cu electrodes formed on the top surface of a microfabricated 100-nm-thick Mn_3Sn single crystal (see Fig.1). An electric current was applied along the [2110] axis and the voltage was measured between electrodes aligned along the [0110] axis, perpendicular to the current. If current inside Mn_3Sn generated spin accumulation with a component parallel to the NiFe magnetization, it would shift the electrochemical potential across the Mn_3Sn/NiFe interface and can therefore be detected as a voltage between NiFe and the Cu electrodes. A rectangular resistance–magnetic field (R–B) hysteresis loop corresponding to the switching of NiFe magnetization is expected for a fixed polarization direction of the accumulated spins. Such a rectangular R–B hysteresis loop was observed in the magnetic-field dependence of the transverse voltage between NiFe and the Cu electrodes. The results in **a** and **b** were obtained after saturation of Mn_3Sn with a sufficiently large magnetic field B of −0.75 T

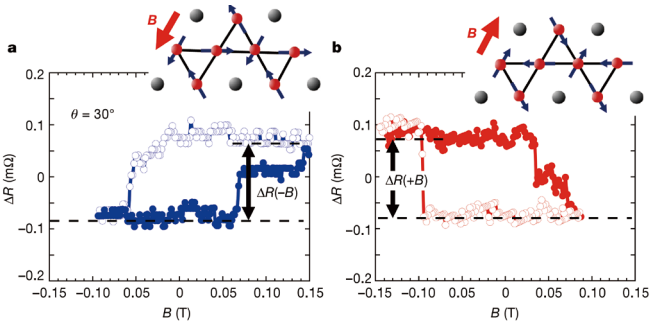

Fig. 2. Spin-accumulation signal. **a**, **b**, Magnetic-field dependence of resistance measured between the NiFe and Cu electrodes at room temperature. The results in aand bwere obtained after saturation of Mn3Sn with a sufficiently large magnetic field Bof −0.75 T and +0.75 T, respectively. The corresponding spin structures of Mn3Sn are shown in the insets.

and +0.75 T, respectively, which provide evidence that the rectangular loops originate from spin accumulation at the Mn_3Sn surface. The key observation in this work is that the spin accumulation signal changes indicate when the Mn_3Sn sub lattice moments are reversed, as illustrated in the inset. This unexpected sign change demonstrates that the dominant contribution to the SHE in Mn_3Sn is odd under time reversal. We find that in the non-collinear antiferromagnet Mn_3Sn, the SHE has an anomalous sign change when its triangularly ordered moments switch orientation. This discovery expands the horizons of antiferromagnet spintronics and spin–charge coupling mechanisms.

References
[1] S. Nakatsuji *et.al*., Nature **527**, 212 (2015)
[2] M. Kimata *et.al*., Nature **565**, 627 (2019)

Authors
Y. Otani, H. Isshiki, M. Kimata, H. Chen[a], K. Kondou[b], S. Sugimoto, P. K. Muduli, M. Ikhlas, Y. Omori, T. Tomita, A. H. MacDonald[a], and S. Nakatsuji
[a]University of Texas at Austin
[b]RIKEN-CEMS

Lithium-Ion Conductivity in Single Crystals of $Li_{10}GeP_2S_{12}$

Hiroi Group

The all-solid-state lithium-ion battery has been studied extensively as a next-generation secondary battery. It uses a solid instead of a liquid electrolyte, which enables to achieve greater safety, higher energy density, wider temperature range of operation, and larger output power compared with the conventional battery. To realize this, an efficient Li-ion conductor is required, which exhibits conductivity that is either comparable to or larger than that of commercially used organic liquid electrolytes. $Li_{10}GeP_2S_{12}$ (LGPS) is a promising candidate for the super ionic conductor; compared to other candidates, it has the highest conductivity of 12 mS cm^{-1} at room temperature and an outstanding electrochemical performance in Li batteries [1,2]. Thus, LGPS is a key compound in the materialization of the all-solid-state battery.

The high Li-ion conductivity of LGPS has been ascribed to its specific crystal structure shown in Fig. 1a. There are four partially occupied Li sites inside the rigid framework composed of the tetrahedral units of $Ge_{0.5}P_{0.5}S_4$ and PS_4. Among them, the Li1, Li3, and Li4 sites are located in the distorted tetrahedra of S, while the Li2 site is in the distorted octahedron of S. It has been shown that the Li diffusion between the former sites is crucial for the high conductivity, while the Li2 ions are almost immobile.

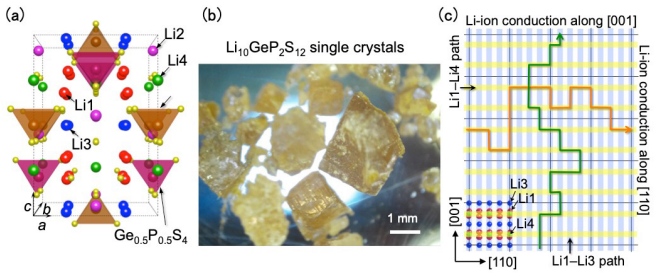

Fig. 1. (a) Crystal structure of $Li_{10}GeP_2S_{12}$ (LGPS), (b) photograph of typical LGPS crystals of a few millimeters in size, and (c) schematic drawing illustrating the possible conducting paths of Li ions in LGPS. The one-dimensional channel via the Li1–Li3 path along the *c* axis is dominant, and a two-dimensional hopping via the Li1–Li4 path in the <110> direction is secondary in the short-range Li-ion conduction. However, the actual long-range conduction occurs via such meandering paths as shown by the green and orange lines in (c), which give rise to weakly anisotropic Li-ion conductivity.

A highly anisotropic ion diffusion has been proposed based on neutron diffraction (ND) measurements and molecular dynamics calculations: a one-dimensional (1D) channel via the Li1–Li3 path along the *c* axis is dominant, and a two-dimensional (2D) hopping via the Li1–Li4 path in the <110> direction is secondary [3]. The activation energies of the local hopping processes for the 1D and 2D paths are determined as 0.16 (0.17) and 0.26 (0.28) eV from the NMR experiments (the molecular dynamics calculations), respectively. Thus, considerable anisotropy can be expected in the atomic-scale diffusion process. In contrast, pulsed-field gradient NMR measurements, which may be sensitive to long-range Li diffusion at the micrometer scale, suggests a nearly isotropic Li diffusion.

An impedance measurement using a single crystal provides important information with which to clarify the origin of this difference and the mechanism of ion diffusion in LGPS. However, because of the lack of a sufficiently large single crystal, the Li diffusion in the bulk had not been measured thus far. Previous impedance measurements using polycrystalline samples yielded an average conductivity of ~10 mS cm^{-1} and activation energy of 0.22–0.28 eV. Understanding of the true conduction mechanism in LGPS is crucial for the improvement of LGPS and for further development of a better solid electrolyte for the all-solid-state battery. In the present study, we obtain large single crystals of LGPS, a few millimeters in size, using the self-flux method (Fig. 1b), and carry out impedance measurements in the [001] and [110] directions [4]. The conductivity is, in fact, higher along [001] than along [110]; however, the difference is only a factor of 4. In addition, the activation energies are nearly equal for the two directions, suggesting a weak anisotropic 3D diffusion in LGPS, as schematically illustrated in Fig. 1c.

References
[1] N. Kamaya, K. Homma, Y. Yamakawa *et al.*, Nat. Mater. **10**, 682 (2011).
[2] Y. Kato, S. Hori, T. Saito *et al.*, Nat. Energy **1**, 16030 (2016).
[3] X. Liang, L. Wang, Y. Jiang *et al.*, Chem. Mater. **27**, 5503 (2015).
[4] R. Iwasaki, S. Hori, R. Kanno, T. Yajima, D. Hirai, Y. Kato, and Z. Hiroi, Chem. Mater. **31**, 3694 (2019).

Authors
R. Iwasaki, S. Hori[a], R. Kanno[a], T. Yajima, D. Hirai, Y. Kato[b], and Z. Hiroi
[a]Tokyo Institute of Technology
[b]Toyota Motor Corporation

From Gapless Kitaev Spin Liquid to Classical String Gas through Tensor Networks

Kawashima Group

Quantum spin liquids (QSLs) represent a state of quantum matter which is not characterized by any local order parameters even at zero temperature. These novel states are expected to exhibit long-range entanglement leading to the topological order and fractionalized excitations. For example, the Haldane phase, which is known as a symmetry-protected topological phase, is a fascinating phase one can find in the

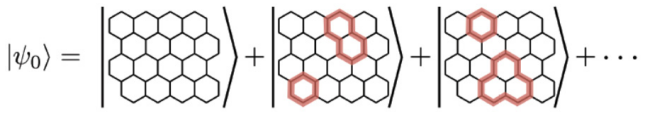

Fig. 1. Schematic representation of the "loop-gas" state. It is a sum of all loop-gas configurations. Each configuration corresponds to a product of Pauli operators. The loop-gas configuration determines which Pauli operator is aligned on a given lattice.

S=1 quantum spin chain. The novel character that discriminates the Haldane phase from trivial gapped states was most clearly revealed by the discovery of Affleck-Kennedy-Lieb-Tasaki (AKLT) model and its exact ground state or the AKLT state. Its compact representation in the form of a matrix-product state provided a new insight into the Haldane phase. As a two-dimensional system with spin-liquid state, the Kitaev model on honeycomb lattice (KHM) is now a subject of active research, due to recent successful realizations of Kitaev materials. The model is exactly solvable and exhibits gapless and gapped Kitaev spin liquid (KSL) ground states with fractionalized excitations.

In the present work, we propose a "loop-gas" state, i.e., an exactly-solvable quantum state that has a compact and exact tensor-network representation, and a series of ansatze that starts from the loop-gas state and converges rapidly to the KHM ground-state. The loop gas state is defined by the loop-gas projector applied to a product state in which all spins are aligned in the (111) direction. The loop-gas projector is defined as tensor-network operator with bond-dimension 2, which is represented by a sum of all loop configurations each corresponding to a product of Pauli operators on all lattice points. (Fig. 1) We find that the norm of the loop gas state is exactly the same as the classical loop gas model at the critical fugacity on honeycomb lattice. The classical loop gas model appears in the low-temperature expansion of the Ising model, and therefore shares the same critical properties as the latter. These observations establishes that the correlation function of the loop-gas state is exactly the same as the correlation function of the critical Ising model. Furthermore, by defining the dimer-gas operator in an analogous way to the loop-gas operator, and applying it to the loop-gas state, we can improve the loop-gas state as an approximate to the KHM ground-state. (Fig. 2) For example, the second order approximation, which is obtained by applying the dimer-gas operator twice, achieves more than 4-digits accuracy in the energy. This is better than any other previous variational wave function. Also, note that there are only two adjustable parameters in the ansatz.

From these results, we conclude that the series of ansatze

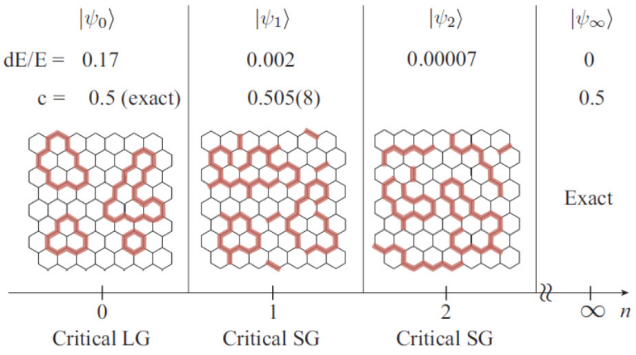

Fig. 2. The series of ansatze converging to the exact KHM ground-state. The zero-th one is the loop-gas state. The energy of the second order approximation already attains 4-digit accuracy, which has never been achieved by other numerical variational methods.

starting from the loop-gas state correctly reflects the essential properties of the family of KSLs, which is known to belong to the Ising universality class. Since the present description of KSLs does not rely on the mapping to fermions, it provides us with an alternative view point to discuss KSLs.

Reference
[1] Hyun-Yong Lee, Ryui Kaneko, Tsuyoshi Okubo and Naoki Kawashima: arXiv:1901.05786.

Authors
H.-Y. Lee, R. Kaneko, T. Okubo[a], and N. Kawashima
[a]Department of Physics, University of Tokyo

Evolution of Magnetic Double Helix and Quantum Criticality Near a Dome of Superconductivity in CrAs

Uwatoko Group

The study of unconventional superconductivity (SC) is one of the most vigorous research fields in condensed matter physics. Although the underlying mechanisms for the unconventional SC in cuprate, iron-based, and heavy-fermion superconductors remains elusive, extensive investigations over the last decades have evidenced quantum criticality as a candidate mechanism for these diverse classes of superconductors. The phase diagrams of these materials often feature a superconducting dome situated adjacent to a magnetically ordered state, with the optimal superconducting transition temperature (T_c) located near a quantum critical point. The close proximity of SC to magnetic order makes it important to elucidate the nature of magnetism.

Recently, we found CrAs as the first superconductor among Cr-based compounds. The transport measurements indicated that the development of SC is accompanied by the suppression of double-helical magnetic order that is coupled with a first-order isostructural transition at ambient pressure. These observations make CrAs an ideal platform for in-depth studies on how the coupled structural and helimagnetic orders are tuned to the critical point and how the magnetism is coupled to the unconventional SC developed nearby. In combinations of elastic and inelastic neutron scattering, resistivity, and specific-heat measurements on undoped CrAs

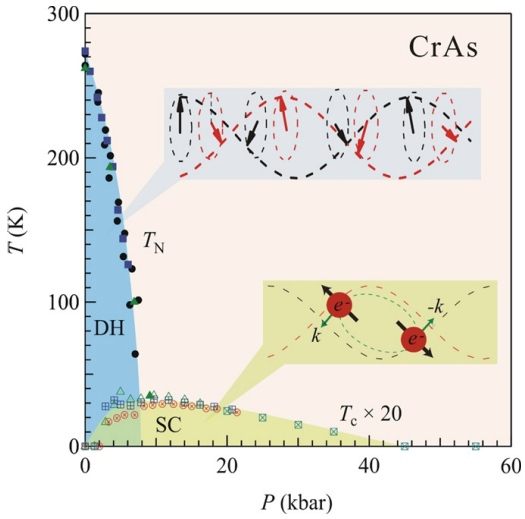

Fig. 1. Pressure dependencies of the double helical (DH) magnetic transition temperature TN and the superconducting (SC) transition temperature Tc for CrAs. Schematic views of the DH structure and Cooper pairing are illustrated in the figure.

and P-doped $CrAs_{1-x}P_x$ single crystals and powders, we have studied systematically the evolutions of static helical order and dynamic spin correlations as well as the electronic properties of CrAs when its coupled structural/helical order is suppressed by either external pressure or the chemical substitutions.

Neutron diffraction on the single-crystal CrAs under hydrostatic pressure (P) shows that the combined order is suppressed at $P_c \approx 10$ kbar, near which bulk superconductivity develops with a maximal transition temperature $T_c \approx 2$ K. We further show that the coupled order is also completely suppressed by phosphorus doping in $CrAs_{1-x}P_x$ at a critical $x_c \approx 0.05$, above which inelastic neutron scattering evidenced persistent antiferromagnetic correlations, providing a possible link between magnetism and superconductivity. In line with the presence of antiferromagnetic fluctuations near P_c (x_c), the A coefficient of the quadratic temperature dependence of resistivity exhibits a dramatic enhancement as P (x) approaches P_c (x_c), around which $r(T)$ has a non-Fermi-liquid form. Accordingly, the electronic specific-heat coefficient of $CrAs_{1-x}P_x$ peaks out around x_c. These properties provide clear evidences for quantum criticality, which we interpret as originating from a nearly second-order helimagnetic quantum phase transition that is concomitant with a first-order structural transition.

We propose that these results can be understood in terms of a proximity to a magnetic quantum critical point tuned by the degree of the incipient localization of the Cr-3d states, possibly via an orbital-selective Mottness mechanism. Our findings in CrAs highlight the distinct characteristics of quantum criticality in bad metals, thereby bringing out new insights into the physics of unconventional SC such as occurring in the high-T_c iron pnictides.

References

[1] W. Wu, J.-G. Cheng, K. Matsubayashi, P. P. Kong, F. K. Lin, C. Q. Jin, N. L. Wang, Y. Uwatoko, and J. L. Luo, Nature Communications **5**, 5508 (2014) .

[2] M. Matsuda, F. K. Lin, R. Yu, J.-G. Cheng, W. Wu, J. P. Sun, J. H. Zhang, P. J. Sun, K. Matsubayashi, T. Miyake, T. Kato, J.-Q. Yan, M. B. Stone, Qimiao Si, J. L. Luo, and Y. Uwatoko, Phys. Rev. X **8**, 031017 (2018).

Authors

M. Matsuda[a], F. K. Lin[b], R. Yu[c], J.-G. Cheng[b], W. Wu[b], J. P. Sun[b], J. H. Zhang[b], P. J. Sun[b], K. Matsubayashi, T. Miyake[d], T. Kato, J.-Q. Yan[a], M. B. Stone[a], Qimiao Si[e], J. L. Luo[b], and Y. Uwatoko

[a]Oak Ridge National Laboratory

[b]Institute of Physics, Chinese Academy of Sciences

[c]Renmin University

[d]Nanosystem Research Institute, AIST

[e]Rice University

High-T_c Superconductivity up to 55 K under High Pressure in a Heavily Electron-Doped $Li_{0.36}(NH_3)_yFe_2Se_2$ Single Crystal

Uwatako Group

To find out the approaches to raise the critical temperature T_c of unconventional superconductors is one of the most enduring problems in contemporary condensed matter physics. The principal route to raise the T_c of FeSe is to dope electron, which has been successfully achieved via the interlayer intercalations [$A_xFe_{2-y}Se_2$ (A = K, Rb), $A_x(NH_3)_yFe_2Se_2$, and (Li,Fe)OHFeSe], interface charge transfer, surface K dosing, and gate-voltage regulation. Further enhancement of T_c via adding more electrons seems to be plagued by the observed insulating state in the over doped regime. Given the limitations of electron doping, it is imperative to explore other routes to enhance T_c of these heavily electron doped (HED) FeSe materials further. In contrast to electron-doping approaches, the application of high pressure can provide an alternative means.

In this work [1], we had performed high-pressure measurement on $Li_{0.36}(NH_3)_yFe_2Se_2$ single crystal, which can reach an optimal $T_c^{onset} \approx 44.3$ K at ambient pressure. From high-pressure resistivity and AC- susceptibility measurement, we can conclude that superconducting transition temperature $T_c \approx 44$ K at ambient pressure is first suppressed to below 20 K upon increasing pressure to $P_c \approx 2$ GPa above which the pressure dependence of $T_c(P)$ reverses and T_c increases steadily to 55 K at 11 GPa. These results thus evidence a pressure-induced second high-T_c superconducting (SC-II) phase in $Li_{0.36}(NH_3)_yFe_2Se_2$ with the highest $T_c^{max} \approx 55$ K among the FeSe-based bulk materials. Also it is evident that the SC-II phase is bulk in nature for 6 GPa, whereas the sample contains two superconducting phases with different Tc above 6 GPa: The high-Tc (50K) phase has a small but nearly constant volume fraction~30% to 11 GPa, whereas the low-(33K) phase shrinks and vanishes completely T_c above 11 GPa.

Figure 1 summarizes the pressure dependences of T_c^{onset} T_c^{zero}, and T_c^{χ} for $Li_{0.36}(NH_3)_yFe_2Se_2$ together with the T_c^{zero}, of FeSe for comparison. The temperature-pressure phase diagram depicts explicitly the evolution of the superconducting phase of $Li_{0.36}(NH_3)_yFe_2Se_2$ under pressure. The high-T_c SC-1 phase, intitially achived at ambient pressure via doping electron through inserting lithium Li+ and ammonia in between the FeSe layers, is quikly suppressed by pressure, and the supercondiucting phase emerges above $P_c \approx 2$ GPa and exists in a broad pressure range.

To further characterize the SC-II phase, we tentatively probe the information about Fermi surface under pressure by measuring the Hall effect in the normal state just above T_c. Hall data confirms that in the emergent SC-II phase the dominant electron-type carrier density undergoes a fourfold enhancement and tracks the same trend as $T_c(P)$. Interestingly, we find a nearly parallel scaling behavior between Tc and the inverse Hall coefficient for the SC-II phases of

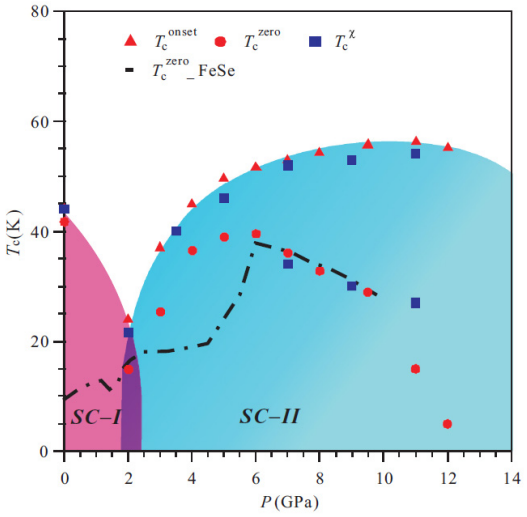

Fig. 1. The T-P phase diagram of the $Li_{0.36}(NH_3)_yFe_2Se_2$ single crystal. The pressure dependence of the superconducting transition temperatures T_c up to 12 GPa.

$Li_{0.36}(NH_3)_yFe_2Se_2$.

Our present study thus demonstrates a way for high pressure to raise T_c of these HED FeSe-based materials by increasing the effective charge-carrier concentration via a possible Fermi-surface reconstruction at P_c.

Reference

[1] P. Shahi, J.P. Sun, S.H. Wang, Y.Y. Jiao, K.Y. Chen, S.S. Sun, H.C. Lei, Y. Uwatoko, B.S. Wang, and J-G Cheng, Phys. Rev. B, **97**, 020508 (2018).

Authors

P. Shahi[a,b], J.P. Sun[a,b], S.H. Wang[c], Y.Y. Jiao[a,b] K.Y. Chen[a,b], S.S. Sun[c], H.C. Lei[c], Y. Uwatoko, B.S. Wang[a,b], and J-G Cheng[a,b]

[a]Beijing National Laboratory for Condensed Matter Physics and Institute of Physics, Chinese Academy of Sciences'

[b]University of Chinese Academy of Sciences

[c]Beijing Key Laboratory of Opto-electronic Functional Materials & Micro-nano Devices, Renmin University of China

Thermodynamic and Structural Studies on Super High Entropy Liquids, Alkylated Tetra-phenyl Porphyrins

Yamamuro Group

The fusion (melting) temperature T_{fus} of molecules usually depend on molecular mass M; the larger M is, the higher T_{fus} becomes. For example, T_{fus} of benzene (C_6H_6, M = 78) is 279 K while that of biphenyl (C_6H_5-C_6H_5, M = 154) is 342 K. This is because the intermolecular van der Waals interaction is larger in the crystalline phase with better molecular packing than that in the liquid phase with worse packing.

Recently, Nakanishi group in NIMS found a series of large molecules which exist in liquid states at room temperature. These molecules have π-conjugated cores such as pyrene, naphthalene, anthracene, fullerene, phthalocyanine and long alkylchains bonded to the cores [1]. We consider that these alkylated molecules are stabilized by the large entropy effect which is caused by the conformational disorder of alkylchains. This situation is similar to that of ionic liquids which are in liquid states in spite of their strong inter-ionic interactions. We collectively call this type of liquids "super-high entropy liquids (SHEL)". The physico-chemical properties of SHEL have not been studied well. As the first target we have taken 2,5-C_6C_{10}-tetraphenylporphyrin (2,5-C_6C_{10}-TPP) and 3,5-C_6C_{10}-tetraphenylporphyrin (3,5-C_6C_{10}-TPP). The molecular structure of 2,5-C_6C_{10}-TPP is shown by the inset of Fig. 1; two -O-C_6C_{10} groups are bonded symmetrically to a benzene ring in 3,5-C_6C_{10}-TPP. It is quite interesting that T_{fus} of the alkylated molecules (2,5-C_6C_{10}-TPP, M = 2538) is lower than T_{fus} of non-alkylated molecules (TPP, M = 615, T_{fus} = 723 K).

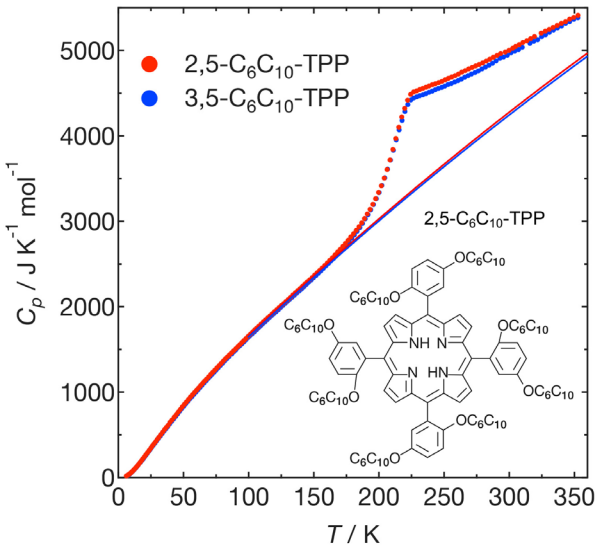

Fig. 1. Heat capacities of 2,5-C_6C_{10}-TPP and 3,5-C_6C_{10}-TPP. The inset shows the molecular structure of 2,5-C_6C_{10}-TPP.

We have measured the heat capacities of 2,5-C_6C_{10}-TPP and 3,5-C_6C_{10}-TPP by use of an adiabatic calorimeter in our lab. The C_p plot shown in Fig. 1 revealed that both molecules have a broad glass transition at around T_g = 210 K and the C_p of 2,5-C_6C_{10}-TPP is 2-3 % larger than that of 3,5-C_6C_{10}-TPP at above T_g. The configurational entropies calculated from the C_p data are more than 1000 $JK^{-1}mol^{-1}$ at high temperature limit, which is more than 10 times larger than those of usual molecular liquids. We have also measured the X-ray diffraction of 2,5-C_6C_{10}-TPP and 3,5-C_6C_{10}-TPP using a diffractometer at BL04B2, SPring-8. Figure 2 shows the reduced pair-correlation function $G(r)$ calculated from the diffraction data; a similar result is obtained in 3,5-C_6C_{10}-TPP. Most of the $G(r)$ peaks are attributed to the C-C correlations in alkylchains. The broad peak at 9 Å, maybe also at 4.5 Å, is considered to be the correlation between porphyrin rings. The present data suggest that the configurations of alkylchains and porphyrin rings of 2,5-C_6C_{10}-TPP and 3,5-C_6C_{10}-TPP are highly disordered at higher temperatures and becomes ordered at lower temperatures. Now we are measuring the quasielastic neutron scattering of both samples to investigate the dynamics of both alkylchains and porphyrin cores.

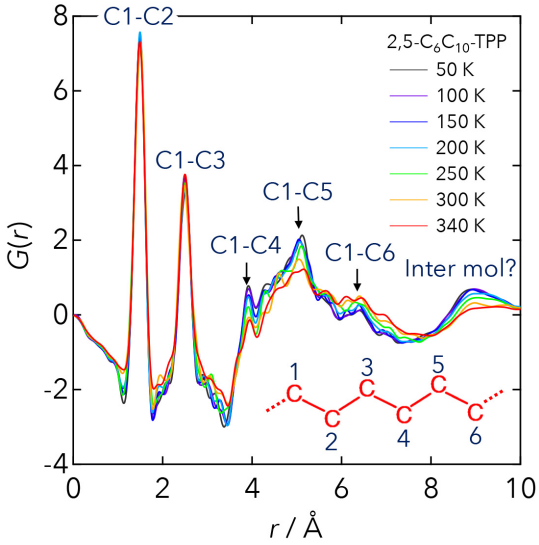

Fig. 2. Temperature dependence of the reduced pair distribution functions of 2,5-C_6C_{10}-TPP calculated from the X-ray diffraction data. The distances corresponding to the intra and intermolecular correlations are given in the figure.

References

[1] A. Ghosh and T. Nakanishi, Chem. Commun. **53**, 10344 (2017).

[2] A. Ghosh, M. Yoshida, K. Suemori, H. Isago, N. Kobayashi, Y. Mizutani, Y. Kurashige, I. Kawamura, M. Nirei, O. Yamamuro, T. Takaya, K. Iwata, A. Saeki, K. Nagura, S. Ishihara, and T. Nakanishi, Nature Chem., submitted.

Authors

M. Nirei, H. Akiba, A. Ghosh[a], T. Nakanishi[a], K. Ohara[b], S. Kohara[a], and O. Yamamuro

[a]NIMS

[b]JASRI

Magnetic States of Coupled Spin Tubes with Frustrated Geometry in $CsCrF_4$

Masuda Group

When a theoretical model is realized in nature, small perturbation terms play important roles in the selection of the ground state in geometrically frustrated magnets. In case of a triangular spin tube, the two-dimensional network of the inter-tube interaction forms characteristic lattices. Among them Kagome-Triangular (KT) lattice in Fig. 1(a) is known to exhibit an enriched phase diagram [1] including various types of non-trivial structures: non-coplanar cuboc structure, coplanar 120° structure with the two-dimensional propagation vector of $\mathbf{k}_{2D} = 0$, $\sqrt{3}\times\sqrt{3}$ structure with $\mathbf{k}_{2D} = (1/3, 1/3)$, and incommensurate structure as shown in Fig. 1(b). We investigate the magnetic state in the model material $CsCrF_4$ in Fig. 1(c) and 1(d) by using neutron diffraction technique. Temperature evolution of the diffraction profile was collected as shown in Fig. 2(a). Combination of representation analysis and Rietveld refinement reveals that a very rare structure, i.e., a quasi-120° structure with $\mathbf{k}_{2D} = (1/2, 0)$ in Fig. 2(b), is realized at the base temperature. The classical calculation of the phase diagram elucidates that $CsCrF_4$ is the first experimental realization of the KT lattice having ferromagnetic Kagome bond. A single-ion anisotropy and Dzyaloshinskii-Moriya interaction play key roles in the selection of the ground state. Furthermore, a successive phase transition having an intermediate state represented by $\mathbf{k}_{2D} = (1/3, 1/3)$ is observed. The intermediate state is a partially ordered 120° structure in Fig. 2(c) [2].

This study was originally initiated for the neutron study of the Tomonaga-Luttinger liquid predicted in a spin tube using JRR-3 research reactor before east Japan earthquake in 2010. Since the magnetic state is sensitive to impurity in the titled compound, we need to check the reproducibility of the data carefully. As a result, the quality of some samples used

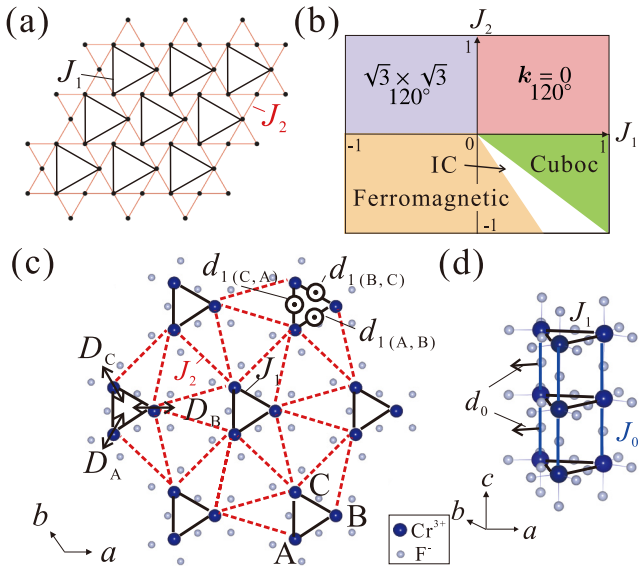

Fig. 1. Coupled spin tubes with frustrated geometry. (a) Kagome-Triangular (KT) lattice. J_1 is the Triangular bond and J_2 is the Kagome bond. (b) Phase diagram of the KT lattice. (c), (d) The crystal structure of $CsCrF_4$. Blue and small gray circles represent Cr^{3+} and F^- ions, respectively. J_1 is the Triangular bond and J_2 is the Kagome bond. The $\mathbf{d}_{1(\{\alpha,\beta\})}$ is DM vector (α,β = A,B,C). z^A, z^B, and z^C are the z-axes locally defined on the Cr sites, A, B, and C. Spin tube runs along the c axis in (d), and the tubes form the KT lattice in the a - b plane in (c).

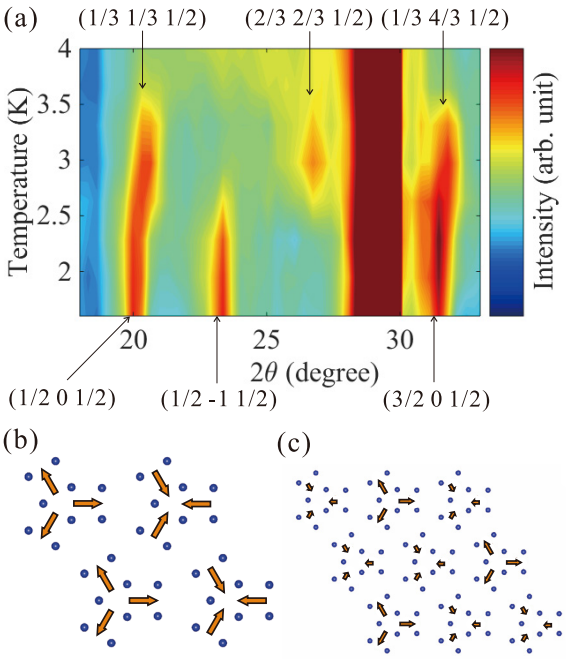

Fig. 2. Magnetic neutron diffraction profile and magnetic structures. (a) The temperature variation of diffraction profiles in the range of 2θ = 18°-33°. (b), (c) Candidates of the magnetic structures of $CsCrF_4$ for the ground state (b) and the intermediated state (c).

at JRR-3 were not good, and we needed to redo the experiment on selected high-quality sample using foreign neutron facilities after 2010. All of the published data in Ref. [2] were, thus, collected at ECHIDNA spectrometer in ANSTO Australia. Furthermore, the difficulty of the transportation of radioactive material such as Cs after the earthquake made the situation complicated. Thanks to many people including scientists, technicians, and office staff, we completed the project.

References
[1] H. Ishikawa *et al.*, J. Phys. Soc. Jpn **83**, 043703 (2014).
[2] M. Hagihala *et al.*, npj Quantum Materials **4**, 14 (2019).

Authors
M. Hagihala, S. Hayashida, M. Avdeev[a], H. Manaka[b], H. Kikuchi and T. Masuda,
[a]Australian Nuclear Science and Technology Organization
[b]Kagoshima University

Magnetic State Selected by Magnetic Dipole Interaction in Kagome Antiferromagnet $NaBa_2Mn_3F_{11}$

Masuda and Hiroi Groups

Long-range magnetic dipole-dipole (MDD) interaction is ubiquitous in nature. In most bulk magnets, the MDD interaction is not necessarily a primary interaction because its energy scale is much smaller than an exchange interaction. The MDD interaction, however, plays a key role in geometrically frustrated magnets, where the geometry causes macroscopic degeneracy of the magnetic state. For instance, the origin of an exotic monopole state in pyrochlore oxides is explained by the MDD interaction [1]. The frustrated geometry and the MDD interaction are, thus, a good combination for search of a new magnetic state.

In a classical Heisenberg kagome antiferromagnet, the ground state is known to be 120° structure with an infinite

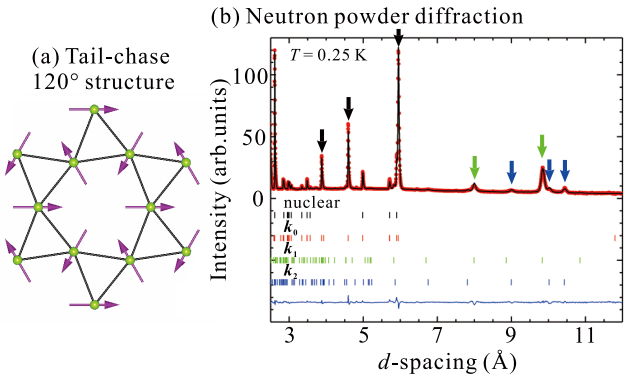

Fig. 1. (a) The tail-chase 120° structure on the kagome lattice. (b) Neutron diffraction profile for $NaBa_2Mn_3F_{11}$ measured at 0.25 K. The solid square and curves show experimental data and simulation, respectively. Arrows indicate magnetic Bragg peaks.

degeneracy. A small perturbation lifts the degeneracy and selects a unique structure, e.g., an all-in all-out structure in case of Dzyaloshinskii-Moriya interaction [2]. The MDD is theoretically predicted to select a *tail-chase* structure (Fig. 1(a)) [3]. Such a structure, however, has not been experimentally identified yet to date. $NaBa_2Mn_3F_{11}$ having a unique kagome-triangular lattice was synthesized by Hiroi group in ISSP [4]. It exhibits an antiferromagnetic transition at T_N = 2 K. The estimated Curie-Weiss temperature of -32 K is smaller than those of many kagome magnets, indicating that the exchange spin interaction is small. The MDD interaction may be important for the determination of the magnetic state.

Recently we carried out neutron powder diffraction experiment to identify the magnetic structure of $NaBa_2Mn_3F_{11}$[5]. We observed magnetic Bragg peaks at 0.25 K as shown in Fig. 1(b). They were indexed by a commensurate magnetic propagation vector $\boldsymbol{k}_0$ = (0,0,0), and two incommensurate vectors $\boldsymbol{k}_1$ = (0.3209,0.3209,0) and $\boldsymbol{k}_2$ = (0.3338,0.3338,0). The magnetic structure analysis by combination of Rietveld refinement and the representation analysis reveals that the tail-chase 120° structure modulated by the incommensurate vectors gives a satisfactory agreement with the experiment. Furthermore, we calculated the phase diagram with the parameters of the nearest- and second-neighbor exchange interaction, and MDD interaction. We identified that the MDD interaction solves the infinite degeneracy and selects the tail-chaise 120° structure in $NaBa_2Mn_3F_{11}$. For the future perspective, the study of magnetic dynamics is beneficial for the search for exotic sates such as zero-energy mode induced by the MDD interaction.

References

[1] J. S. Gardner, M. J. P. Gingras, and J. E. Greedan, Rev. Mod. Phys. **82**, 53 (2010).
[2] M. Elhajal, B. Canals, and C. Lacroix, Phys. Rev. B **66**, 014422 (2002).
[3] M. Maksymenko, V. R. Chandra, and R. Moessner, Phys. Rev. B **91**, 184407 (2015).
[4] H. Ishikawa, T. Okubo, Y. Okamoto, and Z. Hiroi, J. Phys. Soc. Jpn. **83**, 043703 (2014).
[5] S. Hayashida H. Ishikawa, Y. Okamoto, T. Okubo, Z. Hiroi, M. Avdeev, P. Manuel, M. Hagihala, M. Soda, and T. Masuda, Phys. Rev. B **97**, 054411 (2018).

Authors
S. Hayashida, H. Ishikawa, Y. Okamoto[a], T. Okubo[b], Z. Hiroi, M. Avdeev[c], P. Manuel[d], M. Hagihala, M. Soda, and T. Masuda
[a]Nagoya University
[b]Department of Physics, The University of Tokyo
[c]Australian Nuclear Science and Technology Organization
[d]ISIS Pulsed Neutron and Muon Source, Rutherford Appleton Laboratory

Indoor World Record of 1200 T Achieved by the Newly Installed Electromagnetic Flux Compression Megagauss Generator

Takeyama and Y. H. Matsuda Groups

The megagauss laboratory, ISSP, UTokyo, has a long history of generations of megagauss fields, using electromagnetic flux compression (EMFC) since the original work in the late 1970s led by the Chikazumi and Miura group. The 1000 T project was revisited in 2010 and 2011, supported by the funding of the MEXT for the promotion of the basic science, and since then, we have devoted ourselves to the installation of the megagauss generation system and the technical improvements. Condenser bank units with 20 kV, 2 MJ for the seed feed coils, and two sets of the main condenser bank units, 5 MJ and 2 MJ each with 50 kV charging capability have been incorporated. The system consisting of these condenser modules has been installed, and tuning for operation was recently completed in 2019. The giant collector plates and the load coil clamping units have been placed in antiexplosion chambers. Designs of the instruments were optimized for substantial improvement in the electromagnetic field energy conversion efficiency. Using the newly installed system, we have successfully generated ultra-high magnetic fields reaching 1200 T.

The magnet coil used in the EMFC method is comprised of a single-turn steel outer (primary) coil lined with a copper plate inside (the copper-lined (CL) coil; see Fig. 1) and the so-called liner (a thin metal cylinder, made of copper) which is coaxially set inside the primary coil. A pair of seed field coils set on either side of the primary coil [1]–[3] provides the initial magnetic flux. The liner compresses the magnetic flux and generates megagauss magnetic fields. The EMFC utilizes the electric energy source stored in the condenser bank modules. A record-breaking indoor generation of magnetic field was achieved by discharging 45 kV, 3.2 MJ energy out of 5 MJ condenser units. The liner (typical size is 119 mm diameter, 1.5 mm thickness, approximately

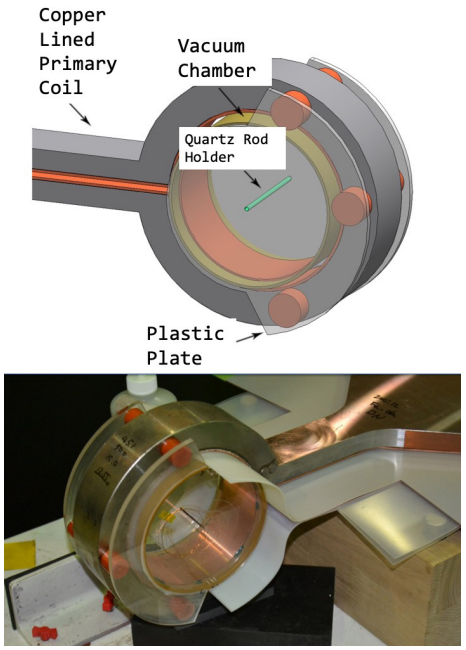

Fig. 1. Overall view of the CL coil and the measurement probe setting. The liner vacuum chamber (made of the Bakelite cylinder and the acrylic resin plastic plates) with the measurement probe is firmly furnished to the CL primary coil with high precision.

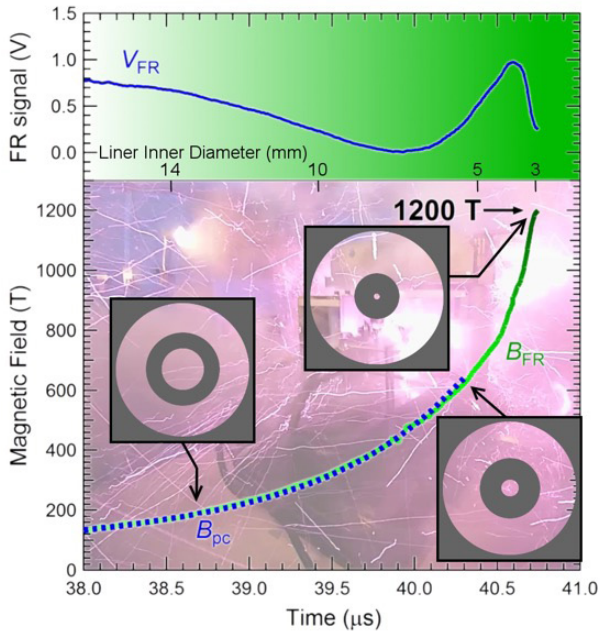

Fig. 2. Magnetic field intensity recorded up to 1200 T with an evolution of time. Upper panel: Faraday rotation signal (V_{FR}) synchronized with the magnetic field intensity. The dotted line taken from the pickup coil (B_{PC}), measured up to 600 T, and the green solid line measures the fields up to 1200 T by FR (B_{FR}). The liner imploding images are shown by black circles. The estimated liner inner diameter at each magnetic field intensity is given in axis of abscissa.

50-mm length) undergoes high-speed implosion (above 5 km/s) accelerated by the magnetic force induced by a huge electric current injected to the primary coil (3–4 mega-Ampere) about its circumference, and the magnetic flux (3.2 T) initially generated in a large volume (diameter 120 mm, length 50 mm) is compressed finally into a small space (3 mm diameter, 20–30 mm length), and reaches a megagauss magnetic field of up to 1200 T. The CL coil was designed to improve the energy transfer efficiency of the imploding liner. The copper lining part bears the current, whereas the massive outer steel coil holds the inertia for the liner acceleration. A liner vacuum chamber with measurement probes are attached to the steel outer coil as shown in Fig. 1. Thus, measurement probes are set precisely at the liner implosion center with respect to the CL coil.

The signals obtained in this work are plotted in Fig. 2. Details are provided in our recent paper [4]. The dotted line is a signal taken from the pickup coil and traced up to 600 T, which is the limit of recording because of the high-voltage induced by the rapid increase of the field. The Faraday rotation signal was intact until the very end of the liner implosion. The green solid line represents the field record after the Faraday rotation signal is converted into the magnetic field intensity. A slow-down effect was observed followed by the peak field prior to the liner "turn-around" phenomenon. Circles depicted in the graph shows images of the liner cross-section during implosion. The liner inner diameter, which corresponds to the bore of the coil, is shown as a guide in the axis of abscissa in the middle of the figure. Final diameter of the liner at 1200 T is estimated to be 3 mm. The maximum speed of the liner during the implosion is estimated to be higher than 5 km/sec, which is consistent with the "Hugoniot curve" [5], in which a field of 1200 T hits at 5.3 km/sec.

References

[1] N. Miura and F. Herlach, Springer Topics in Applied Physics **57**, 247 (Springer, Berlin, 1985).
[2] F. Herlach, Rep. Prog. Phys. **62**, 859 (1999).
[3] N. Miura and F. Herlach, High Magnetic Fields-Science and Technology **1**, 235 (World Scientific, 2002).
[4] D. Nakamura, A. Ikeda, H. Sawabe, Y. H. Matsuda and S. Takeyama, Rev. Sci. Instrum. **89**, 095106 (2018).
[5] F. Herlach, Rep. Prog. Phys.**62**, 859 (1999).

Authors
S. Takeyama, D. Nakamura, H. Sawabe, Y. H. Matsuda, and A. Ikeda.

Determination of "Diracness" in PbTe

Tokunaga Group

One of the hottest research subjects in condensed matter physics is so-called topological materials, in which dynamics of charge carriers are expressed by the relativistic equations of motion that are utilized in research field of high energy physics. Since the relativistic Dirac/Weyl equations show characteristic linear dispersion relation, a great number of experimental and theoretical studies have been devoted to explore the linear dispersion as schematically shown in Fig. 1(a), which is distinguished from the parabolic one shown in Fig. 1(b). This parabolic dispersion, however, is merely the expanded view of the trace in Fig. 1(a) at around the origin. Therefore, argument based only on the appearance of the dispersion is sensuous and insufficient to quantitatively distinguish the Dirac/Weyl system from the others. As the

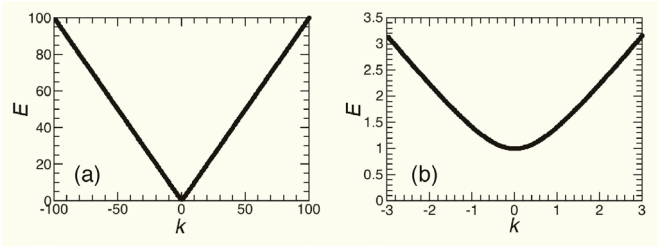

Fig. 1. (a) Schematic dispersion relation of kinetic motion of particles that is expressed by relativistic Dirac equation, which shows characteristic linear dispersion in wide range of the *k*-space. (b) Expanded view the same dispersion relation with that in (a), which appears as parabolic in this region.

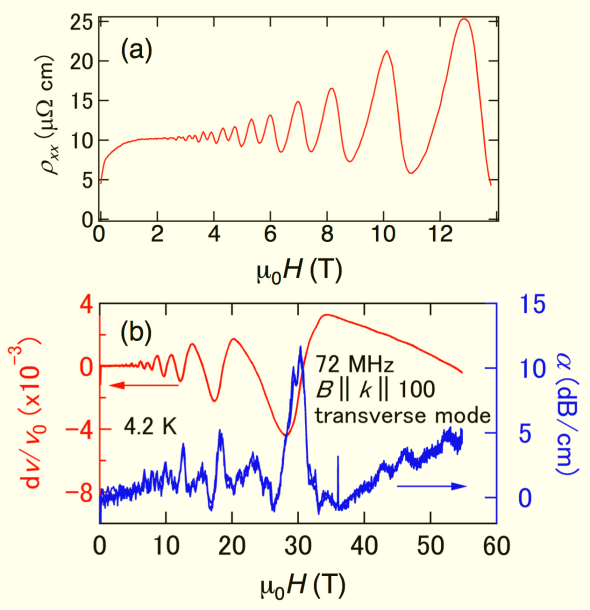

Fig. 2. (a) Transverse magnetoresistance and (b) ultrasound attenuation in single crystals of PbTe. Quantum oscillations are clearly resolved in both experiments.

quantitative indicator that characterizes similarity of a system with the ideal Dirac system, which is called as "Diracness" in the following, we focus on the ratio between Zeeman and cyclotron energies (ZC ratio). Recent theoretical studies revealed that this ZC ratio becomes unity for the ideal Dirac system [1,2]. Relative magnitude of the ZC ratio and unity is predicted to invert when topology of a material changes from trivial to non-trivial.

To experimentally determine the ZC ratio, we studied quantum oscillations in single crystals of PbTe through measurements of magnetoresistance (Fig. 2(a)), magnetization, and ultrasound attenuations (Fig. 2(b)) in DC and pulsed high magnetic fields [3]. By measuring quantum oscillations up to the quantum limit state and comparing the results with the standard Lifshitz-Kosevich formula [4], we determined the ZC ratio of PbTe as 0.52. In this analysis, we clarified that when the ZC ratio becomes larger than one half, peak-dip relation in the quantum oscillation will be reversed, which will appear as the phase shift in the Landau level fan diagram. The results demonstrate that observation of spin-split quantum oscillations is crucially important to discuss the origin of the phase shift.

References

[1] Y. Fuseya *et al*., Phys. Rev. Lett. **115**, 216401 (2015).
[2] H. Hayasaka and Y. Fuseya, J. Phys.: Condens. Matter **28**, 31LT01 (2016).
[3] K. Akiba *et al*., Phys. Rev. B **98**, 115144 (2018).
[4] D. Shoenberg, *Magnetic Oscillations in Metals* (Cambridge University Press, 1984).

Authors

K. Akiba, A. Miyake, H. Sakai[a,b], K. Katayama[a], H. Murakawa[a], N. Hanasaki[a], S. Takaoka[a], Y. Nakanishi[c], M. Yoshizawa[c], and M. Tokunaga

[a]Osaka University
[b]JST-PRESTO
[c]Iwate University

Short-Range Spin Correlations in a Quantum Magnet Detected Through Magnetoelasctic Couplings in a Kagome Quantum Spin Lattice

Y. H. Matsuda, Takeyama, and Hiroi Groups

In case of quantum magnets, magnetostriction can be a unique measure of short-range spin correlations. The spin components perpendicular to the external magnetic field is inherent in the local spin correlation. In quantum magnets, magnetostriction measurement is a direct measure of the local spin correlation.

We have recently developed a high-speed 100 MHz magnetostriction measurement system utilizing the fiber Bragg grating techniques [1] for the use in the μ-seconds pulsed magnetic fields beyond 100 T (megagauss region) and 1000 T (kilo-Tesla region) [2]. We found later that the system can also be used in the milli-seconds pulsed magnetic fields below 100 T with an appreciable high-resolution of $\Delta L/L \sim 10^{-6}$ [3]. Using the developed instrument, we have conducted the magnetostriction measurement for the two-dimensional quantum magnet of volborthite [4].

Volborthite ($Cu_3V_2O_7(OH)_2 \cdot 2H_2O$) is a fascinating example of a highly frustrated quantum magnet. In its magnetic layer, Cu ions possessing spin-1/2 moments form a deformed kagome lattice as schematically shown in Fig. 1(a).

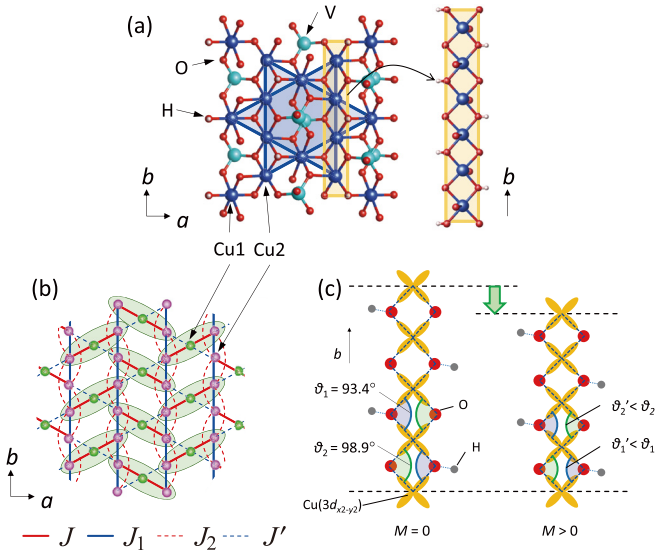

Fig. 1. (a) The lattice model of volborthite (b) Coupled trimer model for volborthite (c) A schematic drawing of the pantograph-like lattice modification of the magnetostriction in the crystallographic *b* axis.

Owing to the lattice deformation, the anisotropic microscopic spin model based on coupled trimers as shown in Fig. 1(b) has recently been proposed, that now attracts attention as it provides a mechanism for a field-induced spin nematic phase adjacent to the 1/3 magnetization plateau. In the spin nematic phase, spin directors that break the in-plane rotational symmetry are formed as a result of the Bose-Einstein condensation of bimagnon excitations. The rotational symmetry breakings take place in the lateral direction of the spin space, which thus implies that the measurement of the lateral spin-correlation in this magnet is quite important.

Figures. 2(a)-(c) shows the result of the magnetostriction

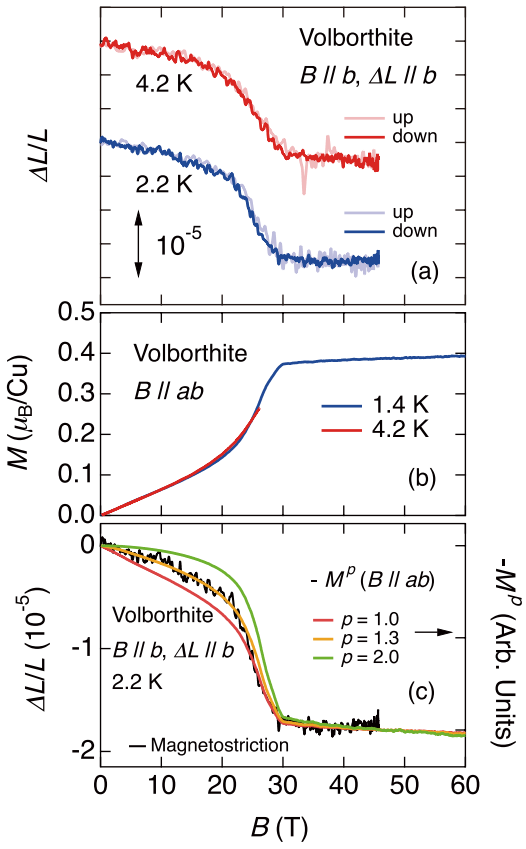

Fig. 2. (a) Magnetostriction curves of volborthite (b) Magnetization curves of volborthite (c) A comparison of the curves of magnetostriction and magnetization indicating a peculiar dependence of $\Delta L \sim M^{1.3}$.

measurement. A negative magnetostriction and a peculiar dependence of the magnetostriction on the magnetization as $\Delta L \sim M^{1.3}$ are observed. The negative magnetostriction in the crystallographic *b* axis is understandable with a pantograph-like lattice modification. As shown in Fig. 1(c), the Cu-O-Cu chain in the *b* axis is responsible for the ferromagnetic superexchange interaction in the coupled trimer model. The closer the bond angles to 90 degree, the stronger the ferromagnetic exchange couplings due to the Kanamori-Goodenough rule, where, as a result, the bond length in the *b* axis is elongated. The story is supported by a tentative DFT+*U* calculations [4]. On the other hand, the peculiar dependence of the magnetostriction on the magnetization can also qualitatively understood as a manifestation of the short-range spin correlation within the exchange striction model. In the exact-diagonalization approach, it becomes clear that the spin-correlation is indeed in between the $M^{1.0}$ and $M^{2.0}$ and close to $M^{1.3}$. For further studies in the future, the spin-nematicity may show abnormal magnetoelastic response at even lower magnetic fields at around 28 T. Another possible study is the measurement beyond 100 T. The end of the 1/3 magnetization plateau may be detected in the magnetostriction measurement.

References

[1] A. Ikeda, T. Nomura, Y. H. Matsuda, S. Tani, Y. Kobayashi, H. Watanabe and K. Sato, Rev. Sci. Instrum. **88**, 083906 (2017).
[2] D. Nakamura, A. Ikeda, H. Sawabe, Y. H. Matsuda, and S. Takeyama, Rev. Sci. Instrum. **89**, 095106 (2018)
[3] A. Ikeda, Y. H. Matsuda, and H. Tsuda, Rev. Sci. Instrum. **89**, 096103 (2018).
[4] A. Ikeda, S. Furukawa, O. Janson, Y. H. Matsuda, S, Takeyama, T. Yajima, Z. Hiroi, and H. Ishikawa, Phys. Rev. B **99**, 140412(R) (2019).

Authors

A. Ikeda and Y. H. Matsuda

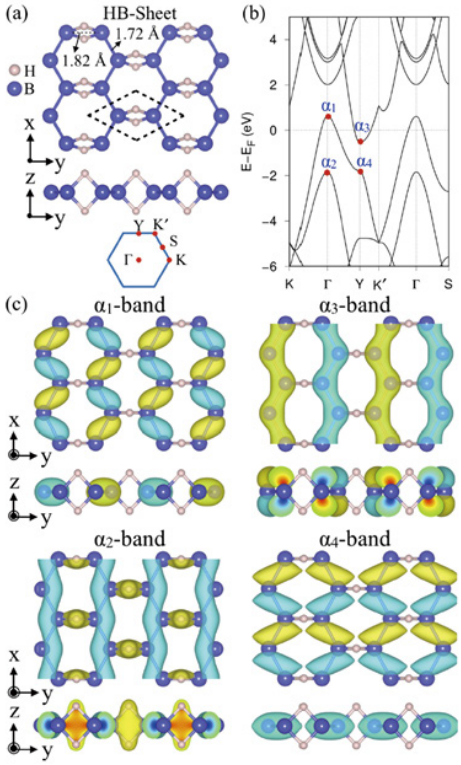

Fig. 1. (a) Atomic structure, and two-dimensional Brillouin zone of a HB sheet. (b) Calculated band structure. (c) Wave function distribution of the α_1-, α_2-, α_3-, and α_4-states. The color of wave functions corresponds to the sign of the periodic part of Bloch wave functions.

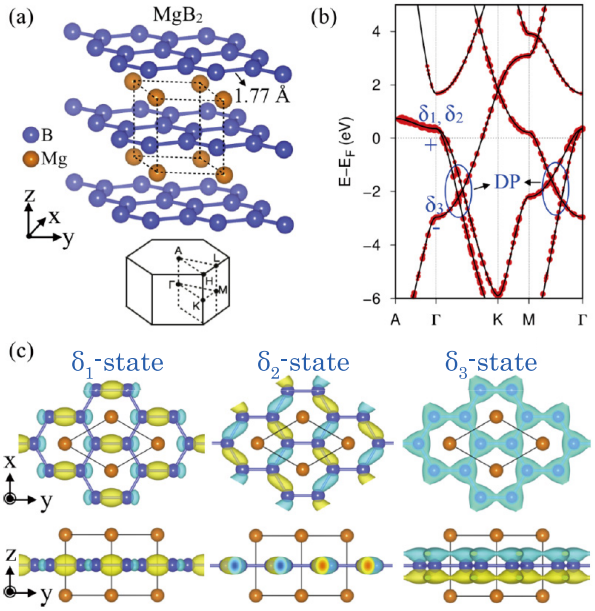

Fig. 2 (a) Atomic structure, and three-dimensional Brillouin zone of a MgB_2 crystal. (b) Calculated band structure. The red dots are the projected band structure of MgB_2 on B atoms. "DP" indicates Dirac point. Dirac points shown in (b) are "cross sections" of Dirac Nodal Loop. (c) Wave function distribution of the δ_1-, δ_2-, and δ_3-states. In (c), the color of wave functions corresponds to the sign of wave functions.

Semi-Metallicity of Free-Standing Hydrogenated Monolayer Boron from MgB_2

I. Matsuda Group

Two-dimensional monatomic layers in van der Waals crystals or on solid surfaces have wide attention because of their unique physical properties and potential applications in quantum devices. There has been growing interests in layers of Xenes. Recently, borophene layers were discovered and found to have Dirac fermions. However, in contrast to graphene, these Xene layers form only on solid surfaces. It is, thus, necessary to develop technique to passivate it chemically so it can be placed on any substrate under ambient conditions.

In the present research, we synthesized a free-standing hydrogenated monolayer boron (HB) sheet and studied the electronic states via soft X-ray spectroscopy at the B K-shell absorption edge and the first-principles calculations [1]. As shown in Fig.1, the HB sheet is semi-metallic with electron and hole pockets at symmetry points of Γ and Y, respectively. The electron band results from the B-H-B bonds formed during synthesis from a MgB_2 crystal, while the hole band is kept through the process and originates from a honeycomb lattice boron layer or borophene in MgB_2. Figure 2 shows a summary of the calculation for a MgB_2 crystal. One can find the one-to-one correspondence between wave-functions of the α_1-state in HB and the δ_2-state in MgB_2. The present research reveals a relation between the surface treatment of monatomic layer and evolutions of the two-dimensional states, giving clues to design novel functional layers.

Reference

[1] I. Tateishi, N. T. Cuong, C.A.S. Moura, M. Cameau, R. Ishibiki, A. Fujino, S. Okada, A. Yamamoto, M. Araki, S. Ito, S. Yamamoto, M. Niibe, T. Tokushima, D.E. Weibel, T. Kondo, M. Ogata, and I. Matsuda, Phys. Rev. Materials **3**, 024004 (2019).

Authors
I. Tateishi[a], N. T. Cuong[b], M. Niibe[c], T. Kondo[b], M. Ogata[a], and I. Matsuda
[a]The University of Tokyo
[b]University of Tsukuba
[c]University of Hyogo

Interfacial Carrier Dynamics of Graphene on SiC, Traced by the Full-Range Time-Resolved Core-Level Photoemission Spectroscopy at SPring-8 BL07LSU

I. Matsuda Group

Time evolutions of the Dirac Fermions in graphene layers have attracted both academic and technological interests due to observations of the various intriguing opto-electric phenomena, such as carrier multiplications and generation of a terahertz laser. Nowadays, graphene layers can be epitaxially grown on a SiC substrate in wide area and such non-equilibrium carriers in the Dirac bands have been directly probed by time-resolved photoemission spectroscopy. On the other hand, the previous studies focused only on electronic evolutions within a graphene layer and little examination was made on carrier dynamics through the graphene/substrate interfaces. Unveiling dynamic roles of the graphene/SiC interface is necessary to understanding the opto-electric properties in SiC based detectors, for example.

In the present research, we conducted measurements of time-resolved core-level photoemission spectroscopy by a combination of laser and synchrotron radiation [1]. The experiment was performed at SPring-8 soft X-ray beamline BL07LSU with the beamline laser station, BL07LASER. Figure 1 shows temporal variations of peak positions of C 1*s* and Si 2*p* during relaxation of the surface photovoltage effect, induced by the optical pumping with a laser pulse. Two C 1*s* components are assigned to a graphene layer (G) and a SiC substrate (SiC), while one Si 2*p* component originates from a SiC substrate. Thus, the high-resolution core-level spectra selectively distinguish dynamical information between overlayer and substrate. While the whole relaxation of the electron-hole recombination process takes 100 nanoseconds, one can also find difference in temporal variation between C and SiC in the subnanosecond region. This is because carrier lifetime in the graphene layers take longer than that of the typical interface-state of SiC by the bottleneck effect of Dirac cones. When there is a buffer layer between graphene and SiC, electron-hole recombination is dominantly held at the interface and the lifetime shortens one-order of the magnitude [1]. The selective evaluations of carrier dynamics in non-uniform samples, such as hetero-junctions, allow one to design and develop novel optoelectric devices.

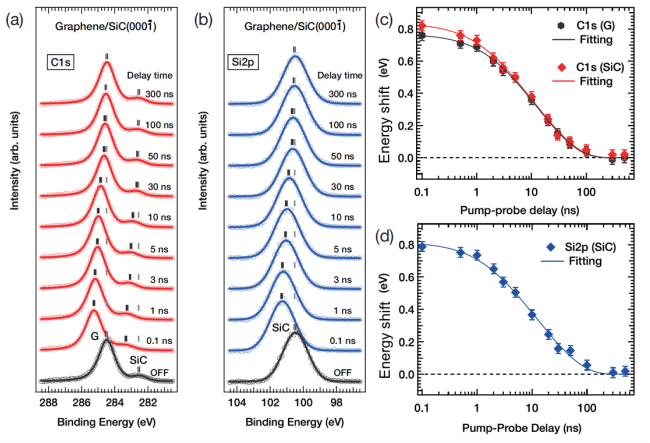

Fig. 1. Time-resolved photoemission spectra for (a) C 1*s* and (b) Si 2*p* core levels of graphene layers on the SiC substrate. In (a), graphene peaks (labeled G) and SiC peaks (labeled SiC) were distinguishably observed. The spectral energy shift measured from the laser OFF was extracted and shown as a function of time for (c) C 1*s* and (d) Si 2*p* core levels.

Reference
[1] T. Someya, H. Fukidome, N. Endo, K. Takahashi, S. Yamamoto, and I. Matsuda, Appl. Phys. Lett. **113**, 051601 (2018).

Authors
H. Fukidome[a], S. Yamamoto, and I. Matsuda
[a]Tohoku University

Polarization Resolved High Harmonic Generation in Semiconducting Gallium Selenide

Itatani Group

Recent progress in ultrafast laser technology has realized to produce strong optical fields in the mid-infrared to terahertz spectral regions. Emergence of such intense long-wavelength light sources triggers ultrafast strong-field physics for condensed matters. When crystalline materials are irradiated by intense mid-infrared pulses, for example, extreme ballistic oscillation of electrons in a conduction band with terahertz to petahertz frequencies occurs, and high-order harmonics are often produced beyond a typical bandgap of solids. So far, most of the experiments employ one-dimensional study along a specific direction. However, we show that a one-dimensional model is not suitable to investigate

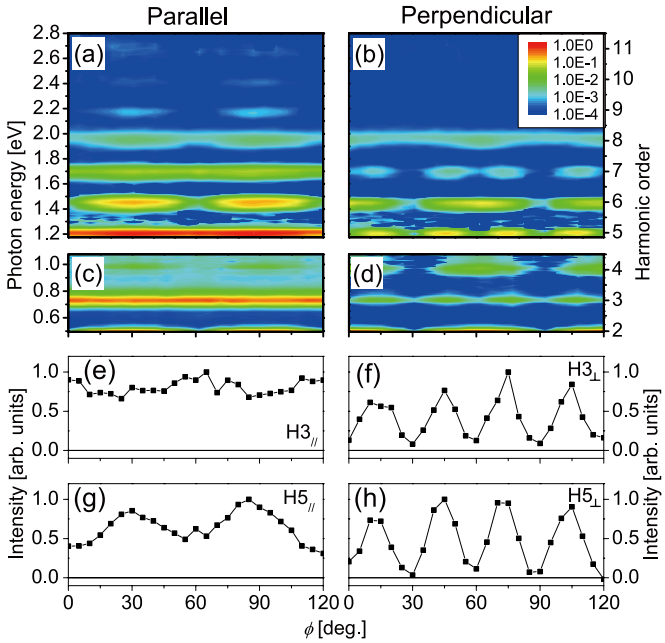

Fig. 1. Polarization resolved measurement of the crystallographic orientation dependence of high harmonics generated in GaSe with a high field amplitude of 10 MV/cm. Parallel (a, visible; c, infrared) and perpendicular (b, visible; d, infrared) polarization components of the high harmonics. Curve plots of the parallel third (e), perpendicular third (f), parallel fifth (g), and perpendicular fifth (h) harmonics.

polarization property of HHG in solids.

In this study, we investigate polarization properties of high harmonics produced in a 30-μm-thick gallium selenide (GaSe, ε-type, [001] z-cut, hexagonal structure, non-coat). The crystal is exposed to linearly polarized femtosecond mid-infrared pulses with a field amplitudes of ~10 MV/cm that are produced from a dual-wavelength optical parametric amplifier (wavelength: 5 μm, maximum pulse energy: 15 μJ, pulse duration: 200 fs, repetition rate: 1 kHz) [1]. The crystallographic orientation dependence of high harmonic spectra is measured after a set of wire-grid polarizers in the either parallel (Fig. 1(a), (c), (e), and (g)) or perpendicular (Fig. 1(b), (d), (f), and (h)) to the mid-infrared field. The observed high harmonics are extended up to the 11th order (2.70 eV, 460 nm) beyond the bandgap (1.98 eV, 625 nm). All even harmonics for both polarizations show modulations with 60° periodicities, which is consistent with the hexagonal structure of a GaSe crystal. In contrast to the even harmonics, the parallel and odd harmonics show 60° modulation on top of a constant offset as in Figs. 1 (e) and (g) for the third and fifth harmonics, respectively. More surprisingly, the perpendicular odd harmonics appear with 30° periodicity as can be seen in Figs. 1(f) and (h). This 30° periodicity cannot be intuitively understood from the hexagonal structure of the crystal.

To explain these results, a two-dimensional single-band model described by the Bloch theorem is used [2]. This model assumes that (i) the intraband current dominates odd harmonics and (ii) the electron wavepacket is launched around the Γ point. Detailed explanation of the model and a verification of these assumptions can be found in Ref. [3]. We found that the band curvature (Figs. 2 (b) and (c)) of the lowest conduction band (Fig. 2(a)) along the electron trajectory is responsible for the source of odd-order harmonics. Based on the two-dimensional single-band model, the parallel and perpendicular odd harmonics are calculated to show 60° and 30° periodicities as can be seen in Figs. 2(d) and (e), respectively. These results well reproduce the experimental observations of the orientation dependences and the polarization property for all odd harmonics.

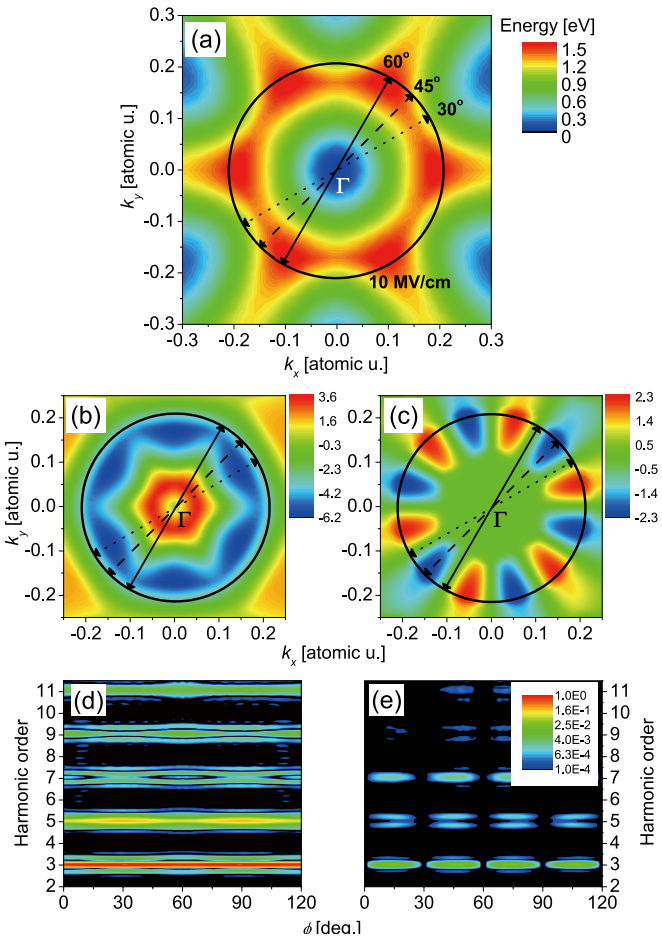

Fig. 2. Calculated results by the two-dimensional single-band model. (a) Lowest conduction band of GaSe and its band curvatures. (b) the band curvature component responsible for parallel odd harmonic generation. (c) the other band curvature component responsible for perpendicular odd harmonic generation. Three electron trajectories at φ = 60° (solid black arrows), 45°(dash), and 30°(dot) are illustrated. The maximum amplitude of electron trajectories with an electric field of 10 MV/cm is shown by the black circle. Orientation dependence of the (d) parallel and (e) perpendicular harmonics obtained by the two-dimensional single-band model with the 10-MV/cm electric field.

In summary, we have investigated a polarization property of high harmonics from a bulk GaSe crystal using femtosecond MIR pulses and their dependence on crystallographic orientation. With the 10 MV/cm electric field, the perpendicular odd harmonic emerges with a periodic modulation of 30°, which cannot be explained by the perturbative nonlinear optics. The underpinned physics of the perpendicular component of the odd harmonics is attributed to anisotropic momentum dependence of the band curvature along the electron trajectory, which is equivalent to the inverse effective mass. Our demonstration establishes a direct link between the band structure and HHG in a crystalline solid. Multi-dimensional analysis combined with time-resolved measurement allows to investigate electron dynamics and field-dressed structure of energy bands in future.

References

[1] K. Kaneshima, N. Ishii, K. Takeuchi, and J. Itatani, Opt. Express **24**, 8660 (2016).
[2] S. Ghimire, A. D. DiChiara, E. Sistrunk, P. Agostini, L. F. DiMauro, and D. A. Reis, Nature Phys. **7**, 138 (2011).
[3] K. Kaneshima, Y. Shinohara, K. Takeuchi, N. Ishii, K. Imasaka, T. Kaji, S. Ashihara, K. L. Ishikawa, and J. Itatani, Phys. Rev. Lett. **120**, 243903 (2018).

Authors

K. Kaneshima, Y. Shinohara[a], K. Takeuchi, N. Ishii, K. Imasaka[b], T. Kaji[b], S. Ashihara[b], K. L. Ishikawa[a, c], and J. Itatani
[a]Photon Science Center, School of Engineering, The University of Tokyo
[b]Institute of Industrial Science, The University of Tokyo
[c]Department of Nuclear Engineering and Management, School of Engineering, The University of Tokyo